Dalton Transactions

Red-emitting neutral rhenium(I) complexes bearing a pyridyl pyridoannelated N-heterocyclic carbene

Journal:	*Dalton Transactions*
Manuscript ID	DT-ART-12-2019-004890.R1
Article Type:	Paper
Date Submitted by the Author:	03-Feb-2020
Complete List of Authors:	Bonfiglio, Anna; Université de Strasbourg, Institut de Physique et Chimie des Matériaux de Strasbourg, UMR 7504 Magra, Kevin; Universite de Lorraine - Site de Metz, Institut de Chimie, Physique et Matériaux (ICPM) Cebrián Ávila, Cristina; Universite de Lorraine - Site de Metz, Institut de Chimie, Physique et Matériaux (ICPM) Polo, Federico; Ca'Foscari University of Venice, Department of Molecular Sciences and Nanosystems Gros, Philippe; UNIVERSITE DE LORRAINE, UMR 7053 L2CM Mercandelli, Pierluigi; Università di Milano, Dipartimento di Chimica Mauro, Matteo; Université Strasbourg, Institut de Physique et Chimie des Matériaux de Strasbourg, UMR 7504

ARTICLE

Red-emitting neutral rhenium(I) complexes bearing a pyridyl pyridoannelated *N*-heterocyclic carbene

Received 00th January 20xx,
Accepted 00th January 20xx

DOI: 10.1039/x0xx00000x

Anna Bonfiglio,[a] Kévin Magra,[b] Cristina Cebrián,[b] Federico Polo,[c] Philippe C. Gros,[b,d] Pierluigi Mercandelli,[e] and Matteo Mauro*,[a]

Two novel rhenium(I) tricarbonyl complexes of general formula *fac*-[Re(**N^C:**)$(CO)_3$X] are herein presented, where **N^C:** is the pyridoannelated N-heterocyclic carbene (NHC) arising from 2-(2-pyridinyl)imidazo[1,5-*a*]pyridinium hexafluorophosphate proligand, namely [pyipy]PF_6, and X being Cl and Br. The synthetic pathway is a *one-pot* reaction that starts from the azolium salt as the NHC source and [$Re(CO)_5$X] to yield the desired charge-neutral *fac*-[Re(**pyipy**)$(CO)_3$X] complexes (**1**–**2**) . Both complexes were thoroughly characterized by spectroscopic, electrochemical, theoretical investigation as well as X-ray diffraction analysis. They display a rather similar electronic absorption spectrum in dilute CH_2Cl_2 solution, which is characterized by a broad profile extending into the blue region. This lowest-lying absorption band is attributed to a transition with admixed metal-to-ligand charge transfer and intraligand charge transfer (^{1}MLCT/^{1}ILCT) character. Degassed samples of the complexes display moderate ($\Phi \approx 1.5\%$) and long-lived (τ = 12.8–13.4 μs) red photoluminescence with highly structured profile independent of the nature of the ancillary halogen ligand and little sensitivity to the solvent polarity, highlighting the markedly different nature of the emitting excited state in comparison with the lowest-lying absorption. Indeed, photoluminescence is ascribed to a long-lived excited state with metal-perturbed triplet ligand-centred (^{3}LC) character as supported by both experimental and density functional theory (DFT) investigations.

Introduction

Phosphorescent complexes have been extensively investigated in the last few decades in the field of organometallic chemistry as well as materials science. In particular, compounds based on second and third row transition metals that feature closed-shell low-spin d^6 electronic configuration, such as Ir(III),[1] Ru(II),[2] Os(II)[3] and Re(I),[4] have attracted a great deal of attention in the recent past owing to their rich redox properties and outstanding photophysics. The presence of the heavy atom induces strong spin-orbit coupling effects to such an extent that the population of the lowest-lying triplet-manifold excited state *via* intersystem crossing processes becomes competitive over other radiative and non-radiative pathways. Following the seminal work of Thompson and Forrest,[5] interest in these classes of photoactive compounds is mainly driven by their application as triplet emitters in light-emitting devices, such as phosphorescent organic light-emitting devices (PhOLEDs).[1,6] More recently, these complexes have found valuable application in photo-catalysis,[7] solar energy conversion,[8] bio-imaging[9] and medicine.[10]

Since the pioneering works of Wrighton[11] and following investigations carried out by other groups,[12-13] tricarbonyl rhenium(I) complexes of general formula *fac*-[Re(**N^N**)$(CO)_3$X]$^{n+}$, where **N^N** is a chelating diimine chromophoric ligand as the archetypical 2,2'-bipyridine or 1,10-phenanthroline, and X is either a neutral (n = 1) or an anionic monodentate ancillary ligand (n = 0), have attracted much interest by the inorganic photochemistry community. These compounds display interesting photophysics and photochemistry mainly arising from a long-lived excited state with triplet metal-to-ligand charge transfer (^{3}MLCT) character, $d\pi(Re) \rightarrow {}^*\pi_{N^N}$. As far as neutral mononuclear species are concerned, they display moderate phosphorescence (PLQY <

[a] *A. Bonfiglio, Dr. M. Mauro*
Université de Strasbourg, CNRS
Institut de Physique et Chimie des Matériaux de Strasbourg
UMR 7504
23 rue du Loess, 67034 Strasbourg (France)
E-mail: mauro@unistra.fr
Homepage URL: http://www.ipcms.unistra.fr/?page_id=31293
[b] *K. Magra, Dr. C. Cebrián, Dr. P. C. Gros*
Université de Lorraine, CNRS, L2CM, F-57000 Metz, France.
[c] *Dr. F. Polo*
Ca' Foscari University of Venice
Department of Molecular Sciences and Nanosystems
Via Torino 155, 30172 Venezia (Italy)
[d] *Dr. P. C. Gros*
Université de Lorraine, CNRS, L2CM, F-5400 Nancy, France
[e] *Prof. P. Mercandelli*
Dipartimento di Chimica, Università degli Studi di Milano, via Camillo Golgi 19, 20133 Milano (Italy)
† See DOI: 10.1039/x0xx00000x

5%) and excited-state lifetime that falls in the order of hundreds of nanoseconds to a few microseconds.[4,11-13]

In contrast to the numerous studies on phosphorescent Re(I)-diimine derivatives, rhenium derivatives bearing stronger σ-donating ligands with coordinating C atoms, such as N-heterocyclic carbene (NHC) type of ligands, have been surprisingly much less explored to date, with only a few reports investigating in detail their photophysics. Notwithstanding, NHCs represent an ubiquitous class of ligands in organometallic chemistry since the discovery of stable NHCs by Bertrand[14] and Arduengo.[15] The popularity of NHCs stems from the peculiar combination of unique features such as strong σ-donating and weak to moderate π-accepting ability and stable M–C bonds. As a consequence, they currently play a pivotal role in transition metal-mediated catalysis,[16] in medicine as chemotherapeutic agents,[17] and in material chemistry.[18] Owing to their appealing electronic and chemical features, NHCs attracted a considerable attention as ligands in the field of phosphorescent emitters as well.[19]

The first report describing the synthesis and photophysical investigation of Re(I)-NHC derivatives in which the NHC acted as the emissive ligand was reported by Massi and co-workers in 2011.[20] The compounds possess the general formula *fac*-[Re(**N^C:**)$(CO)_3$X], where **N^C:** is [3-butyl-1-(2-pyridyl)benzimidazol-2-ylidene] and X is either Cl or Br, and display a moderate and relatively short-lived photoluminescence attributed to an excited state with triplet metal-ligand-to-ligand charge transfer (^{3}MLLCT) character. Since then, a few other reports by the groups of Massi[21] and Barnard[22] described other photoactive Re(I)-NHC complexes bearing either imidazol-2-ylidene or benzimidazol-2-ylidene types of NHC and their potential use as photo-catalysts and radiopharmaceutical agents. Furthermore, a series of rhenium(I) tricarbonyl complexes bearing a pyridyl-NHC ligand was reported by Zheng and co-workers, in which the two coordinating rings were spaced by a methylene bridge.[23] In this latter case, the authors found that the interruption of the conjugation was detrimental, and the complexes resulted to be poorly emissive in both solution and solid state.

Motivated by our interest in luminescent complexes and the possibility to combine the strong metal–ligand interaction, typical of NHC complexes, with the phosphorescence properties of tailored complexes bearing the rhenium(I) tricarbonyl core, we undertook the investigation of a novel class of Re(I) emitters of formula *fac*-[Re(**N^C:**)$(CO)_3$X] (compounds **1–2**) bearing a pyridoannelated NHC as the chromophoric **N^C:** ligand. This chelate features a π-accepting pyridine and an electron-rich σ-donating annelated NHC moiety. The synthesis, chemical, photophysical, electrochemical and computational investigation of two derivatives of this class of complexes are hereafter described. Differently to the results previously reported on related Re-NHC complexes,[20] complexes **1–2** display red ligand-centred (LC) phosphorescence, which does not depend of the nature or the ancillary halogen atom.

Results and discussion

Synthesis and X-ray structure

The two rhenium(I) tricarbonyl complexes of general formula *fac*-[Re(pyipy)$(CO)_3$X], where pyipy is the pyridyl pyridoannelated carbene ligand and X = Cl (**1**) and Br (**2**), were synthesized from 2-(2-pyridinyl)imidazo[1,5-*a*]pyridinium hexafluorophosphate, [Re$(CO)_5$X] and K_2CO_3 as the base in refluxing dry toluene under argon atmosphere. The *one-pot* synthesis is similar to the procedure reported in literature for related complexes.[20] Upon purification by column chromatography, the desired complexes **1–2** were obtained as yellow powders in moderate yield, and they were fully characterized by ^{1}H and ^{13}C NMR, high-resolution mass spectrometry, Fourier-transformed attenuated total reflection infrared spectroscopy (FT-ATR-IR), elemental and thermogravimetric analysis (TGA). The spectra and TGA analysis are displayed in Figure S1-S16 of the Electronic Supporting Information (ESI). The schematic synthetic pathway is displayed in Figure 1.

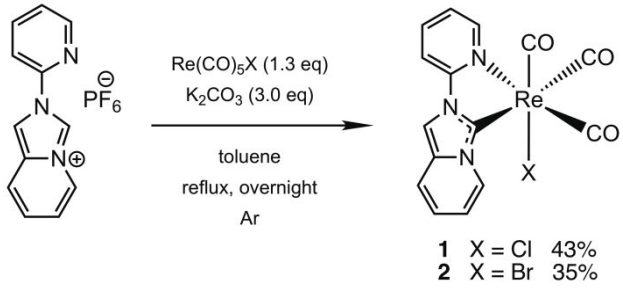

Figure 1. Schematic synthetic pathway employed for the synthesis of complexes **1–2**.

The NMR spectra showed the predicted number of signals expected for the target complexes. Successful coordination of the pyipy ligand was assessed by the downfield shift of the proton resonances observed in the ^{1}H NMR of the pyridine and pyridoannelated moieties when compared to the free ligand precursor (see Figure S1–S10 of the Electronic Supporting Information). In addition, the clear indication of the Re–C_{NHC} bond formation is provided by the complete disappearance of the pro-carbenic proton at δ = 10.17 ppm as well as by the presence of four downfield resonances in the region δ = 185–198 ppm of the ^{13}C NMR spectrum. These latter are attributable to the three C≡O and the carbenic C atoms. Moreover, the formation of the complex with *facial* arrangement of the three carbonyl ligands was supported by FT-IR spectroscopy.[11,24] For complexes **1–2** as neat powder, the vibrational spectra display three intense bands attributable to the C≡O stretching frequencies at $\tilde{\nu}$ = 2006, 1905 and 1874 and 2012, 1914 and 1889 cm^{-1} for compound **1** and **2**, respectively, in agreement with previously reported investigations (see Figure S15–S16). Single crystals of compounds **1–2** grown from slow diffusion of *n*-hexane in acetone were found suitable for X-ray diffractometric analysis that unambiguously confirmed the atoms connectivity (see

Figure 2 and S17 for compound **1** and **2**, respectively). Crystallographic data and some selected geometrical parameters are listed in Table S1–S2 for compound **1** and S3–S4 for compound **2**. Both X-ray structures display a slightly distorted octahedral geometry around the metal centre with the three carbonyl ligands organized in a facial arrangement. As expected, among the three carbonyl ligands, the Re–C bond in *trans* to the carbene possesses the longest distance due to the strong *trans* influence exerted by this latter ligand. Overall, geometrical parameters are in agreement with those Re-NHC structures previously reported.[20-22]

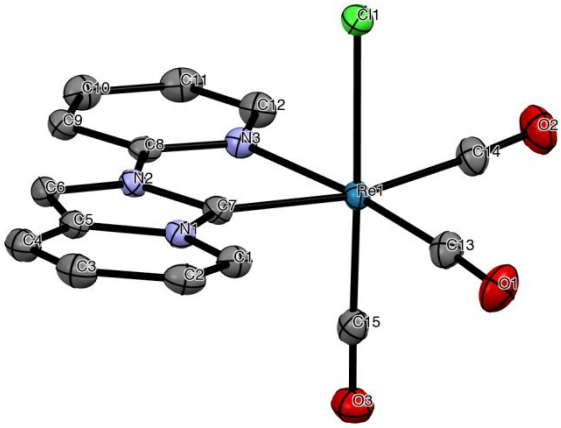

Figure 2. ORTEP diagram of compound **1** with thermal ellipsoids shown at 50% probability level obtained by single-crystal X-ray diffractometric analysis. Hydrogen atoms are omitted for clarity. Selected bond lengths (Å): Re–C(7) = 2.126(2) Å; Re–C(13) = 1.913(2) Å; Re–C(14) = 1.957(2) Å, Re–C(15) = 1.914(2) Å, Re–N(3) = 2.2085(17) Å; Re–Cl(1) = 2.5049(5) Å.

Photophysics

The photophysical properties of complexes **1** and **2** were firstly investigated in dilute (concentration 2×10^{-5} M) CH_2Cl_2 solution in both air-equilibrated and degassed condition at room temperature. Figure 3 displays the electronic absorption and emission spectra and Table 1 summarizes the photophysical data. For both derivatives **1** and **2**, the absorption spectra show nearly identical features, thus only complex **1** will be described in detail hereafter. In the UV range, an intense absorption band shows a $\lambda_{abs,max}$ = 270 nm with $\varepsilon = 13.5\times10^3$ M^{-1} cm^{-1} for **1**, which well corresponds to the absorption profile of the ligand [pyipy]PF_6. Hence, this band is ascribed as a π–π^* transition localized onto the annelated NHC ligand. In the region at λ_{abs} *ca.* 400 nm, two less intense bands are present, yet partially overlapping. The band at $\lambda_{abs,max}$ = 378 nm with $\varepsilon = 3.4\times10^3$ M^{-1} cm^{-1} for complex **1** can be attributed to the singlet-manifold spin-allowed metal-halogen-to-ligand charge transfer (^{1}MXLCT) with $d\pi(Re)p(X) \rightarrow \pi^*_{py}$ nature and described as a single determinant HOMO–1 → LUMO (see TD-DFT calculations below). On the other hand, the lowest energy transition that appears as a shoulder at $\lambda_{abs,max}$ = 430 nm can be ascribed to an electronic transition with admixed metal-to-ligand charge transfer and intraligand charge transfer (^{1}MLCT/^{1}ILCT) character (*vide infra*).

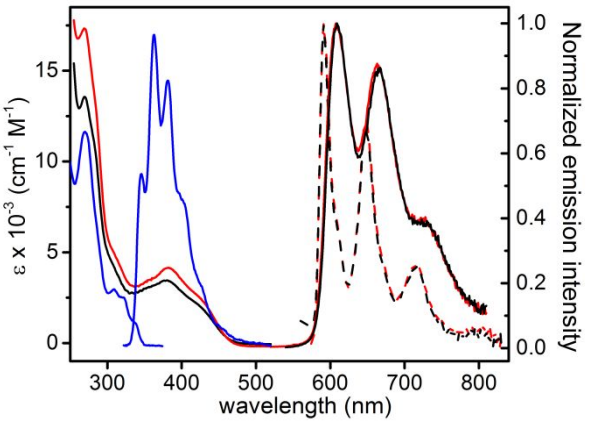

Figure 3. Electronic absorption and photoluminescence spectra of compound **1** (black traces), **2** (red traces) and [pyipy]PF_6 (blue traces) in CH_2Cl_2 solution at a concentration of 2×10^{-5} M at room temperature (solid line) and 77 K (dashed line). Emission spectra were recorded upon excitation at λ_{exc} = 270 and 420 nm, for sample of ligand and complexes, respectively. Spectra of compound **1–2** refer to degassed samples.

The photoluminescence (PL) properties of the complexes were investigated as well, and the corresponding spectra in both degassed and air-equilibrated dilute CH_2Cl_2 are displayed in Figure 3. Upon irradiation at λ_{exc}= 370–420 nm, complexes **1–2** show similar photophysical properties. The photoluminescence spectra proved to be independent of the excitation wavelength, with no evidence of photodegradation for both complexes under the employed experimental condition. Solution samples display a moderate red photoluminescence with a structured profile with maxima at λ_{em} = 608, 664 and 728 nm independently of the presence of dioxygen molecules at room temperature. The pronounced vibronic progression observed in the emission profile features a fundamental spacing in the range of *ca.* 1350 cm^{-1} and it is attributable to intraligand modes. This is further corroborated by the similar spacing observed in the emission spectrum of the ligand [pyipy]PF_6 that displays a structured emission at λ_{em} = 345, 362, 381 and 403 nm (see Figure 3). Degassing the samples yields a sizeable increase of the emission intensity and a prolongation of the excited-state lifetime, being the PLQY of 0.08% *vs* 1.5% and τ = 345 ns *vs* 12.8 µs for complex **1**, respectively. Similar results were obtained for complex **2** and the PL data are summarized in Table 1.[25] This finding clearly supports the triplet nature of the emissive excited state. Furthermore, the two complexes display a large Stokes shift of 4080 and 3800 cm^{-1} for **1** and **2**, respectively.

In sharp contrast to what observed for other classes of luminescent [Re(**N^N**)$(CO)_3$X] complexes characterised by a ^{3}MLCT emission,[26] the absence of any spectral shift upon halogen variation along with the smaller radiative rate constant values (k_r = 1.2×10^3 s^{-1} for complex **1**) and similar vibronic progression observed for both complexes and the [pyipy]PF_6 ligand undoubtedly suggest a ^{3}LC nature of the excited state responsible for the emission process in complexes **1**–**2**.

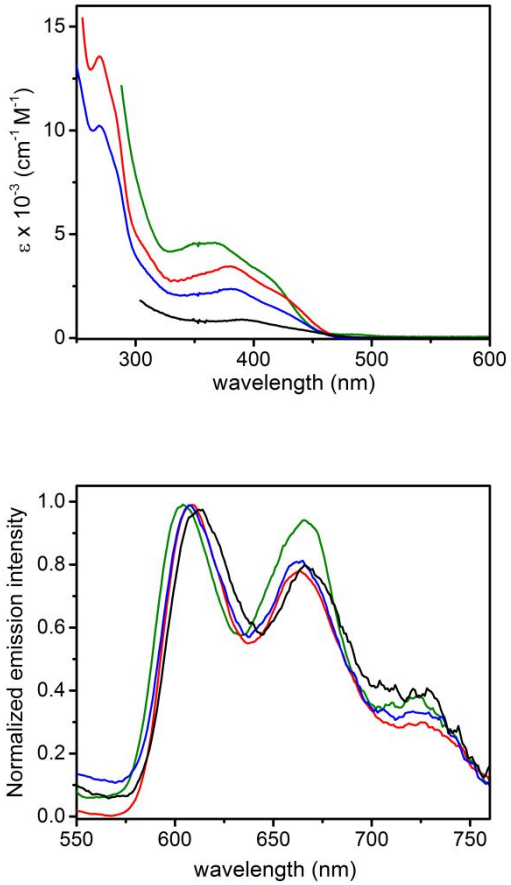

Figure 4. Absorption (*top*) and emission (*bottom*) spectra of diluted samples of complex **1** recorded in solvents with different polarities. DMF (green trace), CH_2Cl_2 (red trace), THF (cyan trace) and toluene (black trace).

Solvent effect experiments were carried out to gain deeper insights onto the nature of the low-lying absorption processes and emitting excited state and to further corroborate our assignments. The spectra recorded in toluene, THF, CH_2Cl_2 and DMF are displayed in Figure 4 and the corresponding data listed in Table 2. Upon increasing solvent polarity, absorption spectra show a negative solvatochromism of the lower-lying band as typical of Re(I) *tris*-carbonyl complexes.[11] On the other hand, the highest energy emission maximum shows a minor shifts from 604 to 614 nm on decreasing solvent polarity, pointing towards a small decrease of the dipole moment when going from the ground to the excited state, and indicating a negligible CT nature of the emissive excited state.

Overall these findings suggest that for both complexes upon excitation into the ^{1}MLCT band excited state relaxation induces a large electronic reorganisation, funnelling the energy into the lowest-lying emissive state with metal-perturbed ^{3}LC character that is localized onto the annelated NHC ligand. This picture is also supported by the DFT calculations (see below).

Table 1. Photophysical properties of complexes **1**–**2** in air-equilibrated and degassed CH_2Cl_2 solution at a concentration of 2×10^{-5} M at room temperature and at 77 K in 2-MeTHF glassy matrix.

Cmpd	$\lambda_{max,abs}$ (ε) [nm, (10^3 M^{-1} cm^{-1})]	λ_{em} [nm]	PLQY (%)		τ_{obs}		k_r [a] [10^3 s^{-1}]	k_{nr} [b] [10^4 s^{-1}]	λ_{em} (77 K) [nm]
			air-equilibrated	*degassed*	*air-equilibrated*	*degassed*			
1	270 (13.5), 378 (3.4), 427*sh* (1.9)	608, 664, 728	0.08	1.5	345 ns	12.8 μs	1.2	7.70	590, 647, 715, 795
2	269 (17.3), 381 (4.1), 429*sh* (2.2)	608, 664, 728	0.06	1.4	297 ns	13.4 μs	1.0	7.36	590, 647, 715, 795

sh denotes a shoulder; [a] k_r = PLQY/τ; [b] k_{nr} = (1 – PLQY)/τ

ARTICLE

Table 2. Solvent effect recorded for complex **1** in solvents of different polarity at a concentration of 2×10^{-5} M at room temperature.

Solvent	$\lambda_{max,abs}$ (ε) [nm, 10^3 M^{-1} cm^{-1}]	λ_{em} [nm]
Toluene	389[a]	614, 671, 732
CH_2Cl_2	270 (13.5), 378 (3.4), 427 (1.9)	608, 664, 728
THF	269 (10.1), 380 (2.3), 425 (1.2)	607, 663, 728
DMF	367 (4.5), 418 (2.6)	604, 665, 724

[a] sample not fully solubilized.

Electrochemistry

The electrochemical behaviour of **1** and **2** was assessed by cyclic voltammetry (CV) in N,N-dimethylformamide (DMF)/0.1 M tetra-*n*-butylammonium perchlorate (TBAP) and showed very similar features (see Figure 5 and Figure S19-S21 of the ESI), as both compounds underwent an irreversible oxidation process (O_1) at E_{ox1} = +1.151 and +1.177 V *vs* SCE, respectively, and one main irreversible reduction process (R_1) at E_{R1} = –1.586 and –1.543 V *vs* SCE, respectively. To better appreciate the redox processes, O_1 and R_1 were recorded separately, and the ligand [pyipy]PF_6 was also investigated to provide the correct peak assignment and as for comparison. The electrochemical data are summarized in Table 3. O_1 occurs at less positive potentials than that of benchmark complex [Re(bpy)$(CO)_3$Cl] owing to the lower π-acidity of the NHC ligand when compared to the pyridine.[27] Reversible oxidation in Re carbonyl complexes is rarely observed. Thus, O_1 is related to the oxidation of the metal-NHC moiety and the only partial contribution of the M–X bond onto the oxidation process is demonstrated by the poor modulation (*ca.* 26 mV) exerted by the halogen ligand in complex **1**–**2**. Computed energetic levels display a similar trend with a 15 meV shallower HOMO computed for **1** when compared to **2** (see computational section and Figure S22 and S26 of the ESI).

On the other hand, R_1 can be ascribed to the one-electron reduction of the cyclometalating ligand, which was less favoured (35–80 mV) than that of the free ligand owing to the more electron-rich nature of this latter upon carbene formation. Moreover, R_1 was observed at more negative values than that of complex [Re(bpy)$(CO)_3$Cl] due to the decreased π-accepting strength of the chelating ligand in compounds **1**–**2**. These findings are in agreement with previous observations described in literature for similar compounds.[28] As shown in Figure S20 for **1** only, although similar observations hold also for **2**, R_1 was then followed by two other irreversible reduction processes, R_2 (at about E_{R2} = –1.900 V) and R_3 (at about E_{R3} = –2.050 V). R_2 could be related to the dissociation of the halide ligand, as previously observed for similar rhenium(I) complexes bearing a bipyridine chelating ligand.[29] Furthermore, it is worth noticing that, once the potential scan is reverted past $R_{2\text{-}3}$ two peaks appeared at –1.2 V (O_2) and 0 V (O_3), respectively (see Figure S20 and Figure S21b). This phenomenon could be ascribed to the oxidation of the complex back to its neutral form (O_2), followed by the formation of a low amount of dimer that undergoes a weak oxidation (O_3), as previously observed.[29]

Table 3. Electrochemical data for compound **1**–**2** obtained by cyclic voltammetry carried out in DMF and 0.1 M TBAP as the supporting electrolyte.

Cmpd	$E_{p/O1}$ [V] [a]	$\Delta E_{p/2/O1}$ [mV] [b]	$E_{p/R1}$ [V] [a]	$\Delta E_{p2/R1}$ [mV] [b]	$E_{p/R2}$ [V] [a]	*gap* [eV]
1	+1.151	46	-1.586	54	-1.889	2.737
2	+1.177	55	-1.543	60	-1.897	2.720
[pyipy]PF_6	-	-	-1.507	88	-	-

[a] Potential values are referred to SCE at the scan rate of 0.1 Vs^{-1}. [b] $\Delta E_{p/2}$ is defined as E_p-$E_{p/2}$, where $E_{p/2}$ is the potential value when the current i is at half its peak value, i_p, for the processes under investigation (O_1 or R_1, respectively).

The effect of the scan rate was investigated over the range 50–500 mV s^{-1}, and the peak current was found to depend linearly on the square root of scan rate for both **1** and **2**, as shown in Figure S11, thus witnessing that the heterogeneous electron transfer process is diffusion-controlled. On the other hand, E_p-$E_{p/2}$ varied in the range of 45–60 mV regardless of the scan rate, while peak potentials shifted towards more positive potentials (by *ca.* 40 mV) for O_1 and more negative potentials (by *ca.* 50 mV) for R_1, for both **1** and **2**. These data are in agreement with the occurrence of a diffusion-controlled heterogeneous electron transfer reaction, followed by a very fast chemical reaction (EC process).[30] It is worth noting that the ratio between the peak currents, i_p, of O_1 and R_1 is very close to ligand [pyipy]PF_6.

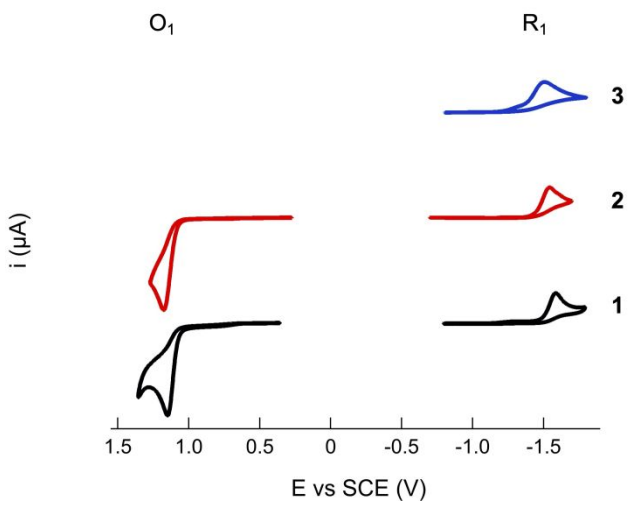

Figure 5. Blank-subtracted CVs recorded for 1 mM of compounds **1** (trace 1), compound **2** (trace 2) and ligand [pyipy]PF_6 (trace 3) in DMF/0.1 M TBAP. Scan rate: 0.1 V s^{-1}.

Computational investigation

To support the interpretation of the photophysical and electrochemical data, the electronic structures of complexes **1** and **2** and their absorption and emission spectra were computed employing density functional (DFT) and time-dependent density functional theory (TD-TDFT). Molecular orbital plots, tables of calculated electronic transition properties, and electron density difference maps are reported in the ESI (Figure S22-S27 and Table S5-S6). The geometrical parameters computed for complexes **1–2** are in good agreement with the corresponding experimental ones, with a mean and maximum unsigned error on bond distances and angles of 0.006 Å and 0.016 Å, and 0.86° and 4.21°, respectively.

Kohn-Sham molecular orbitals in the frontier region are depicted in Figure 6. According to the calculations, the rhenium *d* orbitals in **1** mainly contribute to the four highest occupied molecular orbitals, close lying in energy. The HOMO and HOMO–2 are the two combinations (anti-phase and in-phase, respectively) of one of the *d* orbitals and the highest lying π orbital of the heterocyclic carbene moiety. The HOMO–1 and HOMO–3, on the contrary, do not show contributions from the organic ligand. The HOMO, HOMO–1 and HOMO–2 show, in addition, a significant antibonding interaction with the *p* orbitals of the halogen atom. Lying at lower energy, HOMO–4 is a ligand π orbital extended over both the pyridyl and the heterocyclic carbene rings. The three lowest unoccupied molecular orbitals are π* orbitals delocalized all over the organic ligand. The LUMO+2, in addition, shows a substantial contribution from the carbonyl ligands.

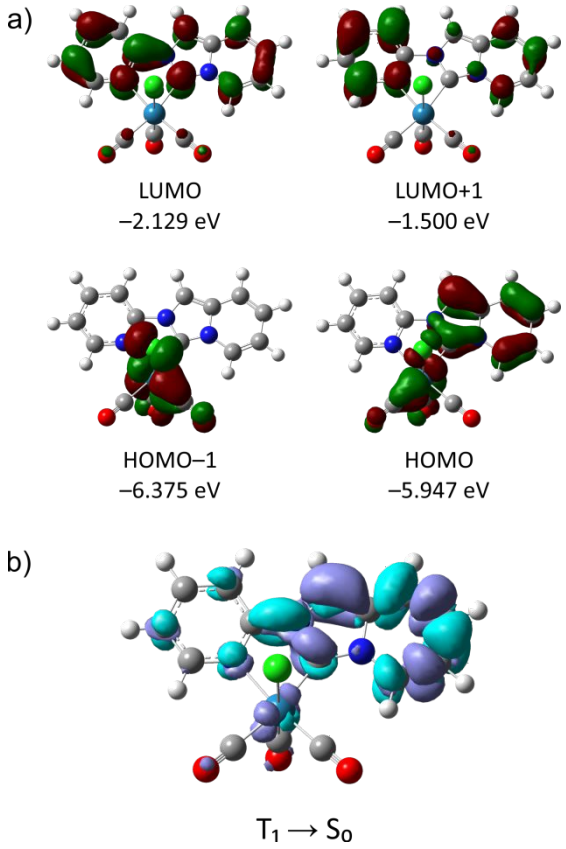

Figure 6. Selected DFT calculation results for compound **1**. (a) Isodensity surface plots and energies computed for the HOMO–1 to LUMO+1 orbitals; (b) electronic density difference maps for the vertical transition $T_1 \rightarrow S_0$, computed at the T_1 at the optimized geometry. Cyan and violet indicates a decrease and increase in electron density, respectively.

TD-DFT calculations were employed to shed a better light onto the nature of the electronic transitions involved in the electronic absorption spectrum. Thus, the band at lower energies in the absorption spectrum of complex **1** can be assigned to the superposition of two electronic transitions, $S_0 \rightarrow S_1$ and $S_0 \rightarrow S_2$ at 416 and 373 nm, corresponding mainly to the HOMO→LUMO and HOMO–1→LUMO monoelectronic excitations, respectively. According to the nature of the orbitals involved, and looking at the corresponding electron density difference maps, both transitions imply a significant metal-halogen-to-ligand charge transfer (^{1}MXLCT) character. The lower-energy transition, however, show also a partial ^{1}ILCT character with a net charge transfer from the heterocyclic carbene ring to the pyridyl moiety. This excitation process involves an electron density displacement that can be overall described as $d\pi(Re)p(X)\pi_{NHC} \rightarrow \pi^*_{N^C}$ (see Table S5 and Figure S22).

Two intense electronic transitions, $S_0 \rightarrow S_{14}$ and $S_0 \rightarrow S_{17}$ at 265 and 255 nm, are responsible for the peak experimentally observed at 270 nm. They correspond to some complex admixtures of many monoelectronic excitations, mainly HOMO–4→LUMO and HOMO–2→LUMO+2. While the first electronic promotion can be described strictly as ligand

centred (^{1}LC), implying a redistribution of the electron density within the pyipy moiety without a net charge transfer between the rings, the second electronic promotion shows a less well-defined nature, since it involves charge transfers both from the $Re(CO)_3Cl$ moiety to the ligand and from the carbene to the pyridyl ring. The complex nature of these transitions can be appreciated also from the corresponding electron density difference maps (Table S5). It is interesting to note that other intense transitions, even higher in energy (down to 230 nm), maintain a similar complex character (see for instance $S_0 \rightarrow S_{21}$ depicted in the ESI).

Geometry optimization of the low-lying triplets for complex **1** leads to the individuation of two triplets, T_1 and T_2. Their geometry differs strikingly: with respect to S_0, T_1 shows an altered alternation of short and long bond lengths within the heterocyclic carbene moiety, leaving the rest of the molecule almost unaltered, while T_2 shows significant modifications of the rhenium–ligand bond lengths, associated with some minor changes within the pyridyl group. According to these geometrical results, and taking into account the electron density difference maps computed for the two vertical transitions $T_1 \rightarrow S_0$ and $T_2 \rightarrow S_0$, the nature of the two triplets can be safely described as ligand centred and metal-to-ligand charge transfer, respectively. Furthermore, the T_1 triplet shows a minor contribution from a rhenium *d* orbital, at variance the halogen ligand p orbitals are not involved.

Both vertical and adiabatic energies have been computed for the $T_1 \rightarrow S_0$ and $T_2 \rightarrow S_0$ transitions. As expected, due to the substantial difference between the triplet and the ground-state geometry, vertical and adiabatic values are quite different (0.384 and 0.487 eV for T_1 and T_2, respectively). The adiabatic energy computed for the $T_1 \rightarrow S_0$ transition slightly underestimates the experimental value (626 vs 608 nm, corresponding to a difference of –0.057 eV or –460 cm^{-1}). The vibrationally resolved emission spectra computed within the framework of the Franck-Condon principle reproduces reasonably well the observed additional maxima (670 and 718 nm vs 664 and 728 nm). As expected for a transition with LC character, the normal modes primarily contributing to the vibronic structure of the band are the intraligand ones, and in particular: ring-ring scissoring (ν_{15}), ring–ring stretching (ν_{19}), ring breathing (ν_{52}) and in-plane ring deformations (ν_{71} and ν_{72}, see ESI).

Results for the bromine derivatives **2** strictly reproduce those already described for the chlorine derivative **1** and they are shown in Figure S26-S27 and Table S6. The only differences are a higher contribution of the bromine p orbitals in the HOMOs of the complex, as a consequence of their higher energy with respect to those of chlorine. This seems to slightly affect the computed absorption transition energies only, resulting in an hypsochromic shift of 2–6 nm, while the computed emission energy remains unaltered, in agreement with the nature of the $T_1 \rightarrow S_0$ transition that does not show contributions from the orbitals of the halogen ligand.

Materials and methods

General considerations

Rhenium pentacarbonyl chloride was purchased from Acros, rhenium pentacarbonyl bromide[31] and the ligand [pyipy]PF_6[32] were prepared accordingly to a procedure published elsewhere. All procedures involving rhenium complexes were carried out under an argon atmosphere using standard Schlenk techniques. Silica gel for column chromatography was purchased from Sigma-Aldrich. Nuclear magnetic resonance spectra were recorded using a Bruker Avance III HD 500 spectrometer equipped with a N_2 cryo-probe CPPBBO Prodigy at 298 K. ^{1}H and ^{13}C{^{1}H} NMR spectra were calibrated to residual solvent signals. Infrared spectra were recorded using a Fourier-transformed attenuated total reflectance infrared (FT-ATR-IR) spectrometer from Perkin Elmer. Elemental analyses were obtained at the AMS Fédération de Chimie Le Bel, University of Strasbourg on a Flash 2000 ThermoFischer Scientific apparatus. Thermogravimetric analysis was performed on a Q50 apparatus of TA Instruments, at a scanning rate of 5 °C min^{-1} and with nitrogen as purge gas. HR-ESI-MS spectra were recorded on a MicroToF Bruker equipped with an electrospray ionization source.

Synthesis

A solution of dry toluene was bubbled with argon for a few minutes prior addition of 3 eq. of K_2CO_3, 1.3 eq. of $Re(CO)_5X$ and 1 eq. of the ligand [pyipy]PF_6. The reaction was refluxed overnight under argon. After cooling, the mixture was extracted with CH_2Cl_2 and distilled H_2O. The organic phase was then dried over Na_2SO_4 and the solvent evaporated. The crude was purified by column chromatography using a mixture of CH_2Cl_2:CH_3CN (10:1) for X = Cl (R_f = 0.5) and pure CH_2Cl_2 for X = Br (R_f = 0.8). The desired products were obtained as yellow powders.

***fac*-[Re(pyipy)(CO)$_3$Cl]** (**1**): (65 mg, 0.13 mmol) 43% yield. ^{1}H NMR (500 MHz, 298 K, CD_2Cl_2) δ: 8.96 (dd, *J* = 5.5, 0.9 Hz, 1H), 8.38 (dd, *J* = 7.3, 0.8 Hz, 1H), 8.11 (td, *J* = 8.2, 1.6 Hz, 1H), 7.94 (s, 1H), 7.83 (d, *J* = 8.3 Hz, 1H), 7.43 (ddd, *J* = 7.4, 5.6, 0.9 Hz, 1H), 7.39 (d, *J* = 9.4 Hz, 1H), 6.99 (dd, *J* = 9.2, 6.5 Hz, 1H), 6.83–6.79 (m, 1H). ^{13}C NMR (125.77 MHz, 298 K, CD_2Cl_2) δ: 199.1, 198.2, 188.3, 185.8, 154.3, 153.4, 141.7, 132.9, 128.8, 125.1, 124.8, 118.2, 116.0, 113.5, 106.5. ESI-MS calcd for $C_{15}H_9ClN_3NaO_3Re$: 523.9773. Found for ([M+Na]$^+$): 523.9769. Anal. calcd for $C_{15}H_9ClN_3O_3Re$: C 35.97 H 1.81 N 8.39. Found C 34.88 H 1.89 N 7.99. FT-ATR-IR (neat powder): 2006(s), 1905(br), 1874(br) (νC≡O) cm^{-1}.

***fac*-[Re(pyipy)(CO)$_3$Br]** (**2**): (55 mg, 0.10 mmol) 35% yield. ^{1}H NMR (500 MHz, 298 K, CD_2Cl_2) δ: 8.97 (dd, *J* = 5.5, 0.9 Hz, 1H), 8.36 (dd, *J* = 7.3, 0.9 Hz, 1H), 8.16–8.12 (m, 1H), 7.94 (s, 1H), 7.84 (d, *J* = 8.3 Hz, 1H), 7.44–7.40 (m, 2H), 7.01 (dd, *J* = 9.3, 6.5 Hz, 1H), 6.83–6.80 (m, 1H). ^{13}C NMR (125.77 MHz, 298 K, CD_2Cl_2) δ: 198.6, 197.6, 187.8, 184.9, 154.5, 153.4, 141.6, 133.0, 128.8, 125.2, 124.7, 118.2, 160.0, 113.5, 106.4. ES-MS calcd for $C_{15}H_9BrN_3KO_3Re$: 583.8998. Found for ([M+K]$^+$): 583.8981. Anal. calcd for $C_{15}H_9BrN_3O_3Re$: C 33.04 H 1.66 N

7.71. Found C 32.46 H 1.71 N 7.48. FT-ATR-IR (neat powder): 2012(s), 1914(br), 1889(br) (νC≡O) cm^{-1}.

X-ray diffractometric analysis

The crystals were placed in oil, and a single crystal was selected, mounted on a glass fibre and placed in a low-temperature N_2 stream. X-ray diffraction data collection was carried out on a Bruker PHOTON III DUO CPAD diffractometer equipped with an Oxford Cryosystem liquid N_2 device, using Mo-Kα radiation (λ = 0.71073 Å). The crystal-detector distance was 37 mm. The cell parameters were determined (APEX3 software).[33] from reflections taken from 1 set of 180 frames at one second exposure. The structure was solved using the program SHELXT-2014.[34] The refinement and all further calculations were carried out using SHELXL-2014.[35] The hydrogen atoms were included in calculated positions and treated as riding atoms using SHELXL default parameters. The non-hydrogen atoms were refined anisotropically, using weighted full-matrix least-squares on F^2. A semi-empirical absorption correction was applied using SADABS in APEX3.[33]

Photophysical characterization

Instrument details. Absorption spectra were measured on a Varian Cary 100 double-beam UV–VIS spectrophotometer and baseline corrected. Steady-state emission spectra were recorded on a Horiba Jobin–Yvon IBH FL-322 Fluorolog 3 spectrometer equipped with a 450 W xenon arc lamp, double-grating excitation, and emission monochromators (2.1 nm mm^{-1} of dispersion; 1200 grooves mm^{-1}) and a Hamamatsu R13456 red sensitive Peltier-cooled PMT detector. Emission and excitation spectra were corrected for source intensity (lamp and grating) and emission spectral response (detector and grating) by standard correction curves. Time-resolved measurements were performed using either time-correlated single-photon counting (TCSPC) or multi-channel scaling (MCS) electronics on the Fluorolog 3. For TCSPC, NanoLEDs lamps (450 nm; FWHM <1.2 ns) with repetition rates between 10 kHz and 1 MHz were used to excite the sample. Instead, a pulsed Xe flash lamp was employed for MCS measurements. The excitation sources were mounted directly on the sample chamber at 90° to a double-grating emission monochromator (2.1 nm mm^{-1} of dispersion; 1200 grooves mm^{-1}) and collected by a PPD 850 single-photon-counting detector. The photons collected at the detector are correlated by a time-to-amplitude converter (TAC) to the excitation pulse. Signals were collected using an IBH DataStation Hub photon-counting module and data analysis was performed using the commercially available DAS6 software (Horiba Jobin-Yvon IBH).

For time resolved measurements, the quality of the fit was assessed by minimizing the reduced χ^2 function and by visual inspection of the weighted residuals. Luminescence quantum yields were measured in optically dilute solutions (optical density <0.1 at the excitation wavelength) and compared to reference emitter by following the method of Demas and Crosby.[36] The $Ru(bpy)_3Cl_2$ complex in air-equilibrated water solution at room temperature was used as reference (PLQY = 0.04).[37] All the solvents were spectrophotometric grade. Dearated samples were prepared by the freeze-pump-thaw technique by using a home-made quartz cuvette equipped with a Rotaflo stopcock.

Electrochemistry setup

Anhydrous *N,N*-dimethylformamide (DMF, Sigma-Aldrich, 99.8 %) and tetra-*n*-butylammonium perchlorate (TBAP, Fluka, 99%) were used as received. The working electrode was a glassy-carbon disk electrode (2 mm diameter, Princeton Applied Research GO224). The electrode was polished as already described elsewhere.[38] Before experiments, the electrode was further polished with a 0.05 µm polycrystalline diamond suspension (Buehler, MetaDI) and electrochemically activated in the background solution by means of several voltammetric cycles at 0.5 Vs^{-1} between the anodic and the cathodic solvent/electrolyte discharges, until the expected quality features were attained.[39] A platinum wire served as the counter electrode and a silver wire, separated from the main electrolytic compartment by a Vycor® frit, was used as a quasi-reference electrode. At the end of each experiment, its potential was calibrated against the ferricenium/ferrocene couple, used as an internal redox standard. In DMF/0.1 M TBAP, ferricenium/ferrocene has a formal potential of 0.464 V against the KCl saturated calomel electrode (SCE),[40] which allows to reference all the potentials against SCE. The cyclic voltammetry (CV) experiments were carried out in DMF/0.1 M TBAP under an Ar atmosphere, using a 1 mM concentration for the electroactive compound. A CHI 760b Electrochemical Workstation (CH Instruments) was used. For the CV experiments, we employed the feedback correction to minimize the ohmic drop between the working and the reference electrodes.

Computational details

Ground state and low-lying triplet geometries were optimized by means of density functional calculations. The parameter-free hybrid functional PBE0[41] was employed along with the standard valence double-ζ polarized basis set 6-31G(d,p) for C, H, Cl, N, and O. For Re and Br the Stuttgart–Dresden effective core potentials were employed along with the corresponding valence triple-ζ basis set and a set of polarization functions on Br ($\alpha_{d,Br}$ = 0.389).[42] All the calculations were done in the presence of solvent (dichloromethane, used in the photophysical characterizations) described by a polarizable continuum model (PCM).[43] The nature of all the stationary points was checked by computing vibrational frequencies and all the geometries were found to be true minima. In order to simulate the absorption electronic spectrum down to 230 nm the lowest 25 singlet excitation energies were computed by means of time-dependent density functional calculations. The vibrationally-resolved emission spectra were simulated in the framework of the Franck-Condon principle,[44] shifting the 0–0

energy to its observed value. All the calculations were done with Gaussian 09.[45]

Conclusions

We described the synthesis and characterization of a novel class of tricarbonyl rhenium(I) complexes that bear a pyridyl pyridoannelated *N*-heterocyclic carbene, namely pyipy, as the chromophoric ligand. For both derivatives the coordination of the NHC chelate was unambiguously confirmed by determining the single-crystal X-ray structure. Differently to what observed for other Re(I)-NHC counterparts reported previously, the complexes investigated herein display a stable and long-lived, ligand-centred, red phosphorescence. Assignments of the nature of the electronic transitions involved in both absorption and emission processes were corroborated by TD-DFT calculations and computed results agreed nicely with experimental findings. The electrochemical properties were investigated as well and cyclic voltammograms feature ligand-centred reduction and metal-NHC centred oxidation processes for both complexes.

Finally, our results demonstrate that the combination of strongly σ-donor and weak π-acceptor NHC ligands in combination with the tricarbonyl Re(I) core provide photoactive complexes with interesting photophysical and redox properties that might be exploitable in different applications.

Conflicts of interest

There are no conflicts to declare.

Acknowledgements

A.B. and M.M. gratefully acknowledge the Université de Strasbourg and CNRS for financial support. The International Centre for Frontier Research in Chemistry (icFRC), and the Labex CSC (ANR-10-LABX-0026 CSC) within the Investissement d'Avenir program ANR-10-IDEX-0002-02 is also acknowledged for funding the PhD fellowship of A.B.. M.M. kindly acknowledges the French Agence Nationale de Recherche (ANR) for the grant ANR-18-CE06-007-01. K.M., C.C. and P.C.G. thank the French Agence Nationale de Recherche (ANR-16-CE07-0013-02). Dr. Benoît Heinrich is kindly acknowledged for performing TGA analyses. The Institut Carnot MICA is kindly acknowledged for support and funding.

Notes and references

‡ ^{1}H-, ^{13}C{^{1}H}-, COSY, ROESY, HMBC and HSQC NMR spectra, HR-ESI-MS spectra, TGA thermograms as well as supplementary photophysical, electrochemical, theoretical and crystallographic data can be found in the Electronic Supplementary Information (ESI). Single-crystal X-ray structure: CCDC 1973530 (compound **1**) and CCDC 1980932 (compound **2**).

1 *Iridium(III) in Optoelectronic and Photonics Applications*, Ed. E. Zysman-Colman, John Wiley & Sons Ltd., **2017**; R. D. Costa, E. Ortí, J. J. Bolink, F. Monti, G. Accorsi and N. Armaroli, *Angew. Chem. Int. Ed.*, 2012, **51**, 8178.
2 S. Campagna, F. Puntoriero, F. Nastasi, G. Bergamini and V. Balzani, *Top. Curr. Chem.*, 2007, **280**, 117.
3 D. Kumaresan, K. Shankar, S. Vaidya and R. H. Schmehl, *Top. Curr. Chem.*, 2007, **281**, 101.
4 A. G. Crosby, *Coord. Chem. Rev.*, 2011, **211**, 163; M. Panigati, M. Mauro, D. Donghi, P. Mercandelli, P. Mussini, L. De Cola and G. D'Alfonso, *Coord. Chem. Rev.*, 2012, **256**, 1621; P. V. Simpson, M. Falasca and M. Massi, *Chem. Comm.*, 2018, **54**, 12429.
5 M. A. Baldo, D. F. O'Brien, Y. You, A. Shoustikov, S. Sibley, M. E. Thompson and S. R. Forrest, *Nature*, 1998, 395, 151; M. A. Baldo, M. E. Thomspon and S. R. Forrest, *Nature*, 2000, **403**, 750.
6 H. Yersin (Ed.), *Highly Efficient OLEDs with Phosphorescent Materials*, Wiley-VCH, Weinheim, **2008**; N. Armaroli and H. J. Bolink (Eds.), *Photoluminescent materials and electroluminescent devices*, *Top. Curr. Chem.*, 2017, **374**; V. Balzani, P. Ceroni and A. Juris, *Photochemistry and Photophysics: Concepts, Research, Applications*, Wiley-VCH, **2014**.
7 J. Twilton, C. Le, P. Zhang, M. H. Shaw, R. W. Evans and D. W. C. MacMillan, *Nat. Rev. Chem.*, 2017, **1**, 52.
8 A. Hagfeldt, G. Boschloo, L. Sun, L. Kloo and H. Petterson, *Chem. Rev.*, 2010, **110**, 6595.
9 C. Caporale and M. Massi, *Coord. Chem. Rev.*, 2018, **363**, 71; Q. Zhao, C. Huang and F. Li, *Chem. Soc. Rev.*, 2011, **40**, 2508.
10 A. Zamora, G. Vigueras, V. Rodríguez, M. D. Santana and J. R Ruiz, *Coord. Chem. Rev.*, 2018, **360**, 34; G. Gasser, I. Ott and N. Metzler-Nolte, *J. Med. Chem.*, 2010, **54**, 3; A. Leonidova and G. Gasser, *ACS Chem Bio.*, 2014, **9**, 2180.
11 M. Wrighton and D. L. Morse, *J. Am. Chem. Soc.,* 1974, **96**, 998; P. J. Giordano, S. M. Fredericks, M. Wrighton and D. L. Morse, *J. Am. Chem. Soc.,* 1978, **100**, 2257; P. J. Giordano and M. Wrighton, *J. Am. Chem. Soc.,* 1979, 101, 2888.
12 J. V. Caspar and T. J. Meyer, *J. Phys. Chem.*, 1983, **87**, 952; J. V. Caspar, T. D. Westmoreland, G. H. Allen, P. G. Bradley, T. J. Meyer and W. H. Woodruff, *J. Am. Chem. Soc.,* 1984, **106**, 3492.
13 L. Wallace and D. P. Rillema, *Inorg. Chem.*, 1993, **32**, 3836; L. Wallace, D. C. Jackman, D. P. Rillema and J. W. Merkert, *Inorg. Chem.*, 1995, **34**, 5210; L. Sackteder, A. P. Zipp, E. A. Brown, J. Streich, J. N. Demas and B. A. DeGraff, *Inorg. Chem.*, 1990, **29**, 4335.
14 A. Igau, H. Grutzmacher, A. Baceiredo and G. Bertrand, *J. Am. Chem. Soc.*, 1998, **110**, 6463.
15 A. J. Arduengo, R. L. Harlow and M. A. Kline, *J. Am. Chem. Soc.,* 1991, **113**, 361.
16 D. Bourissou, O. Guerret, F. P. Gabbaï and G. Bertrand, *Chem. Rev.,* 2000, 100, 39; P. de Frémont, N. Marion and S. P. Nolan, *Coord. Chem. Rev.*, 2009, **253**, 862; W. A. Herrmann and C. Köcher, *Angew. Chem. Int. Ed. Engl.*, 1997, **36**, 2162; E. Peris, *Chem. Rev.*, 2018, **118**, 9988; A. Biffis, M. Baron and C. Tubaro, *Adv. Organomet. Chem.*, 2015, 203.
17 M. Skander, P. Retailleau, B. Bourrié, L. Schio, P. Mailliet and A. Marinetti, *J. Med. Chem.,* 2010, **53**, 2146; S. Bellemin-Laponnaz, *Eur. J. Inorg. Chem.*, 2019, doi: 10.1002/ejic.201900960.
18 M. N. Hopkinson, C. Richter, M Schedler and F. Glorius, *Nature*, 2014, **510**, 485; C. A. Smith, M. R. Narouz, P. A. Lummis, I. Singh, A. Nazemi, C. H. Li and C. M. Crudden, *Chem. Rev.,* 2019, **119**, 84986.
19 T. Sajoto, P. I. Djurovich, A. Tamayo, M. Yousufuddin, R. Bau, M. E. Thompson, R. J. Holmes and S. R. Forrest, *Inorg. Chem.*, 2005, **44**, 7992; C.-F. Chang, Y.-M. Cheng, Y. Chi, Y.-C. Chiu, C.-C. Lin, G.-H. Lee, P.-T. Chou, C.-C. Chen, C.-H. Chang and

C.-C. Wu, *Angew. Chem. Int. Ed.*, 2008, **47**, 4542; N. Darmawan, C.-H. Yang, M. Mauro, M. Taynal, S. Heun, J. Pan, H. Buchholz, P. Braunstein and L. De Cola, *Inorg. Chem.*, 2013, **52**, 10756; C. Yang, F. Mehmood, T. L. Lam, S. L.-F. Chan, Y. Wu, C.-S. Yeung, X. Guan, K. Li, C. Y.-S. Chung, C.-Y. Zhou, T. Zoua and C.-M. Che, *Chem. Sci.*, 2013, **4**, 2630; A. Bonfiglio and M. Mauro, *manuscript submitted*.

20 L. A. Casson, S. Muzzioli, P. Raiteri, B. W. Skelton, S. Stagni and M. Massi, *Dalton Trans.*, 2011, **40**, 11960.

21 J. G. Vaughan, B. L. Reid, S. Ramchandani, P. J. Wright, S. Muzzioli, B. W. Skelton, P. Raiteri, D. H. Brown, S. Stagni and M. Massi, *Dalton Trans.*, 2013, **42**, 14100; P. V. Simpson, I. Casaro, S. Paternoster, B. W. Skelton, M. Falasca and M. Massi, *Chem. – Eur. J.*, 2017, **23**, 6518; T. P. Nicholls, L. K. Burt, P. V. Simpson, M. Massi and A. C. Bissember, *Dalton. Trans.,* 2019, **48**, 12749.

22 C. Y. Chan, P. A. Pellegrini, I. Greguric and P. J. Barnard, *Inorg. Chem.*, 2014, **53**, 10862.

23 X.-W. Li, H.-Y. Li, G.-F. Wang, F. Chen, Y.-Z. Li, X.-T. Chen, Y.-X. Zheng and Z.-L. Xue, *Organometallics*, 2012, *31*, 3829; G.-F. Wang, Y.Z. Liu, X.-T. Chen, Y.-X. Zheng and Z.-L. Xue, *Inorg. Chim. Acta*, 2013, **394**, 488.

24 K. Nakamoto, *Infrared and Raman spectra of inorganic and coordination compounds: part B: applications in coordination, organometallic, and bioinorganic chemistry.* 6th Ed., John Wiley & Sons, Inc., **2008**.

25 The recorded lifetimes were found to be independent of the emission wavelength, while the excitation profiles well overlap with the absorption spectra (see Figure S18 of the ESI).

26 D. J. Stukfens and A. Vlcek Jr., *Coord. Chem. Rev.*, 1998, **177**, 127.

27 F. Paolucci, M. Marcaccio, C. Paradisi, S. Roffia, C. A. Bignozzi and C. Amatore, *J. Phys. Chem. B,* 1998, **102**, 4759.

28 L. Suntrup, S. Klenk, J. Klein, S. Sobottka and B. Sarkar, *Inorg. Chem.,* 2017, **56**, 5771.

29 C. J. Stanton, III, C. W. Machan, J. E. Vandezande, T. Jin and G. F. Majetich. *Inorg. Chem.,* 2016, **55**, 3136.

30 A. J. Bard and L. R. Faulkner. *Electrochemical Methods: Fundamentals and Applications*, 2nd Ed., **2000**, Wiley.

31 S. Schmidt, W. C. Trogler and F. Basolo, *Inorg. Synth.*, 1985, **23**, 41.

32 J. T. Hutt and Z. D. Aron, *Org. Lett,* 2011, **13**, 5256.

33 M86-EXX229V1 APEX3 User Manual, Bruker AXS Inc., Madison, USA, **2016**.

34 G. M. Sheldrick, *Acta Cryst.* 2015*,* **A71**, 3.

35 G. M. Sheldrick, *Acta Cryst.* 2015, **C71**, 3.

36 G. A. Crosby and J. N. C. Demas, *J. Am. Chem. Soc.*, 1970, **92**, 7262; H. Ishida, J.-C. Bünzli and A. Beeby, *Pure Appl. Chem.*, 2016, **88**, 701; C. Würth, M. Grabolle, J. Pauli, M. Spieles and U. Resch-Genger, *Nat. Prot.*, 2013, **8**, 1535.

37 I. Ishida, S. Tobita, Y. Hasegawa, R. Katoh and K. Nozaki, *Coord. Chem. Rev.*, 2010, **254**, 2449.

38 S. Antonello, M. Musumeci, D. D. M. Wayner and F. Maran, *J. Am. Chem. Soc.*, 1997, **119**, 9541.

39 A. B. Meneses, S. Antonello, M. C. Arévalo and F. Maran, *Electroanalysis*, 2006, **18**, 363.

40 S. Antonello, M. Musumeci, D. D. M. Wayner and F. Maran, *J. Am. Chem. Soc.*, 1997, **119**, 9541.

41 Called PBE1PBE in Gaussian. (a) C. Adamo and V. Barone, *J. Chem. Phys.*, 1999, **111**, 6158. (b) J. P. Perdew, K. Burke and M. Ernzerhof, *Phys. Rev. Lett.*, 1996, **77**, 3865. (c) J. P. Perdew, K. Burke and M. Ernzerhof, *Phys. Rev. Lett*., 1997, **78**, 1396.

42 S. Huzinaga, J. Andzelm, M. Kłobukowski, E. Radzio-Andzelm, Y. Sakai and H. Tatewaki, *Gaussian Basis Sets for Molecular Calculations*; Elsevier: Amsterdam, **1984**; p. 23.

43 (a) G. Scalmani, M. J. Frisch, B. Mennucci, J. Tomasi, R. Cammi and V. Barone, *J. Chem. Phys.*, 2006, **124**, 094107; (b) G. Scalmani and M. J. Frisch, *J. Chem. Phys.*, 2010, **132**, 114110.

44 V. Barone, J. Bloino, M. Biczysko and F. Santoro, *J. Chem. Theory Comput.*, 2009, **5**, 540.

45 Gaussian09 (revision D.01), Gaussian Inc., Wallingford, CT, **2013.**

ARTICLE

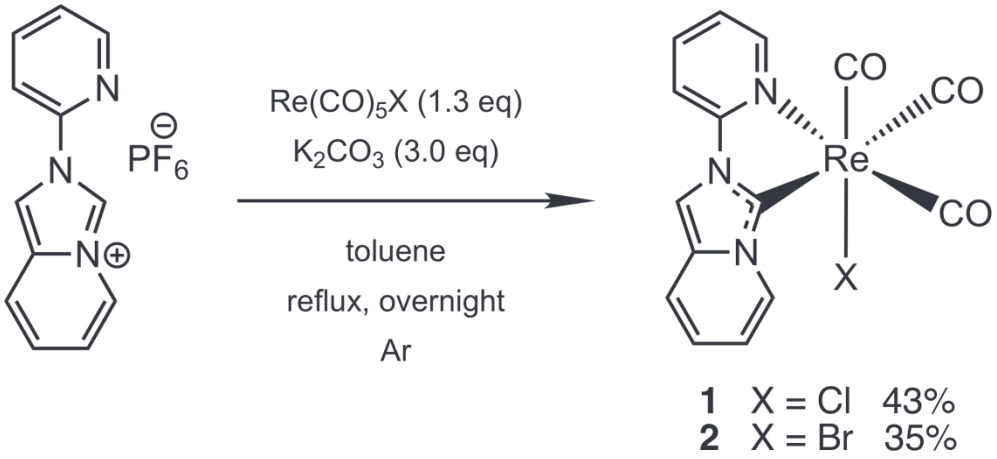

Figure 1 TIFF file

114x52mm (600 x 600 DPI)

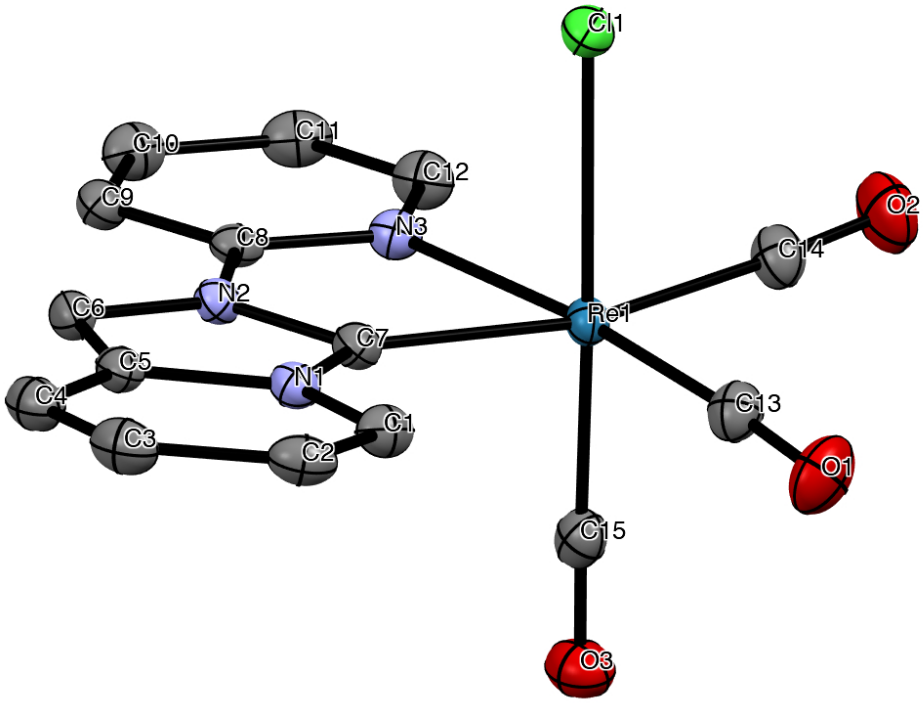

Figure 2

361x270mm (72 x 72 DPI)

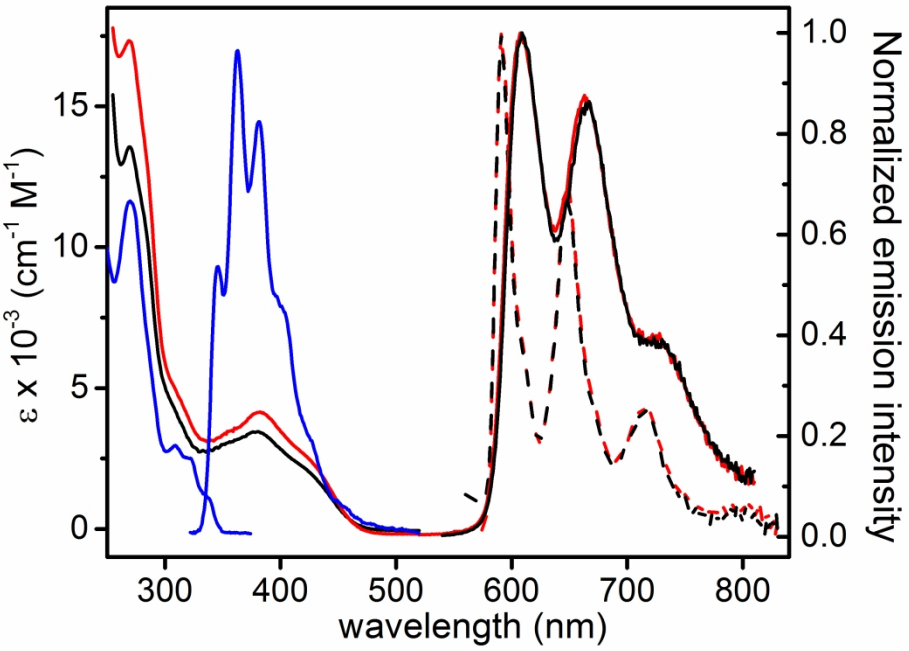

Figure 3

272x208mm (300 x 300 DPI)

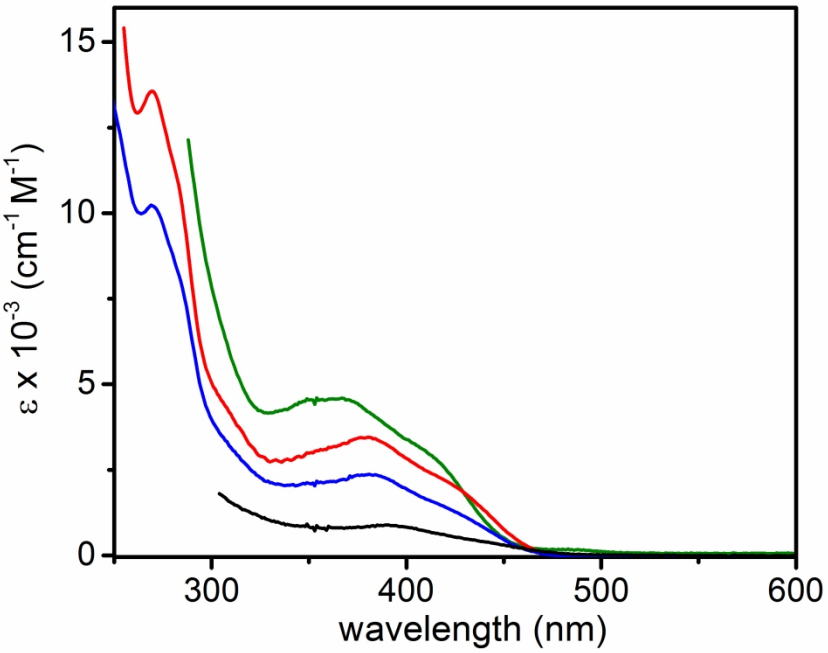

Figure 4 top

272x208mm (300 x 300 DPI)

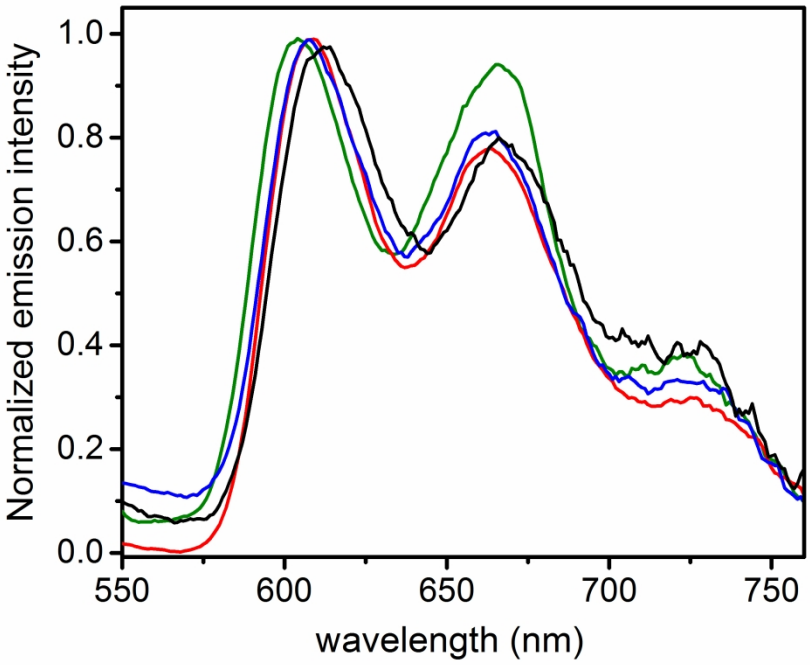

Figure 4 bottom

272x208mm (300 x 300 DPI)

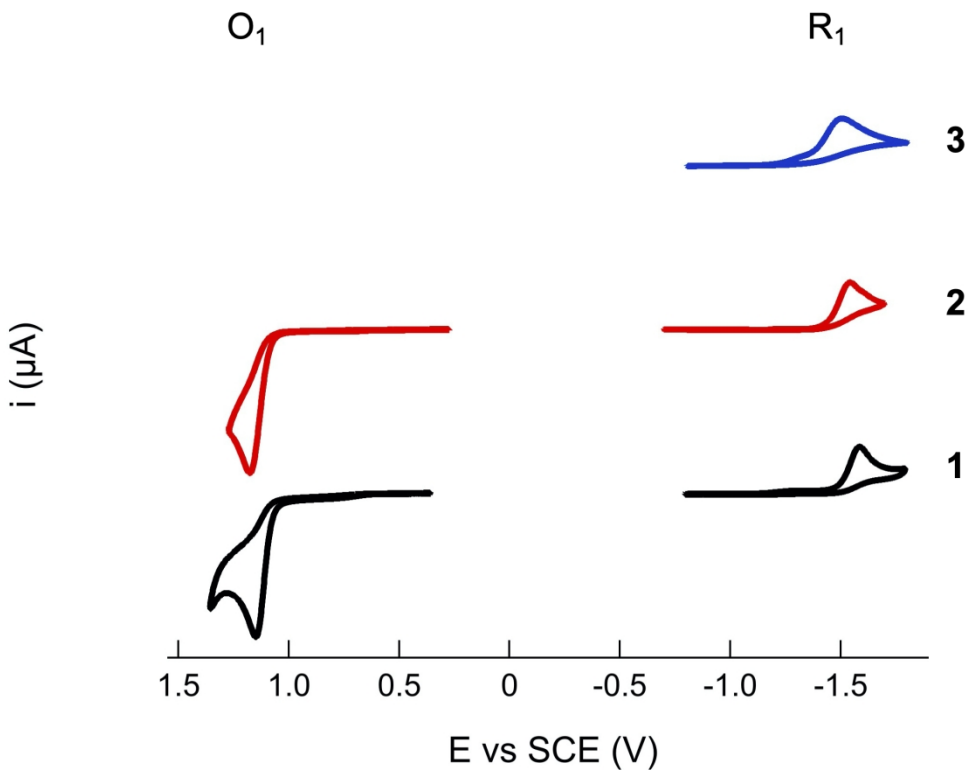

Figure 5

177x138mm (300 x 300 DPI)

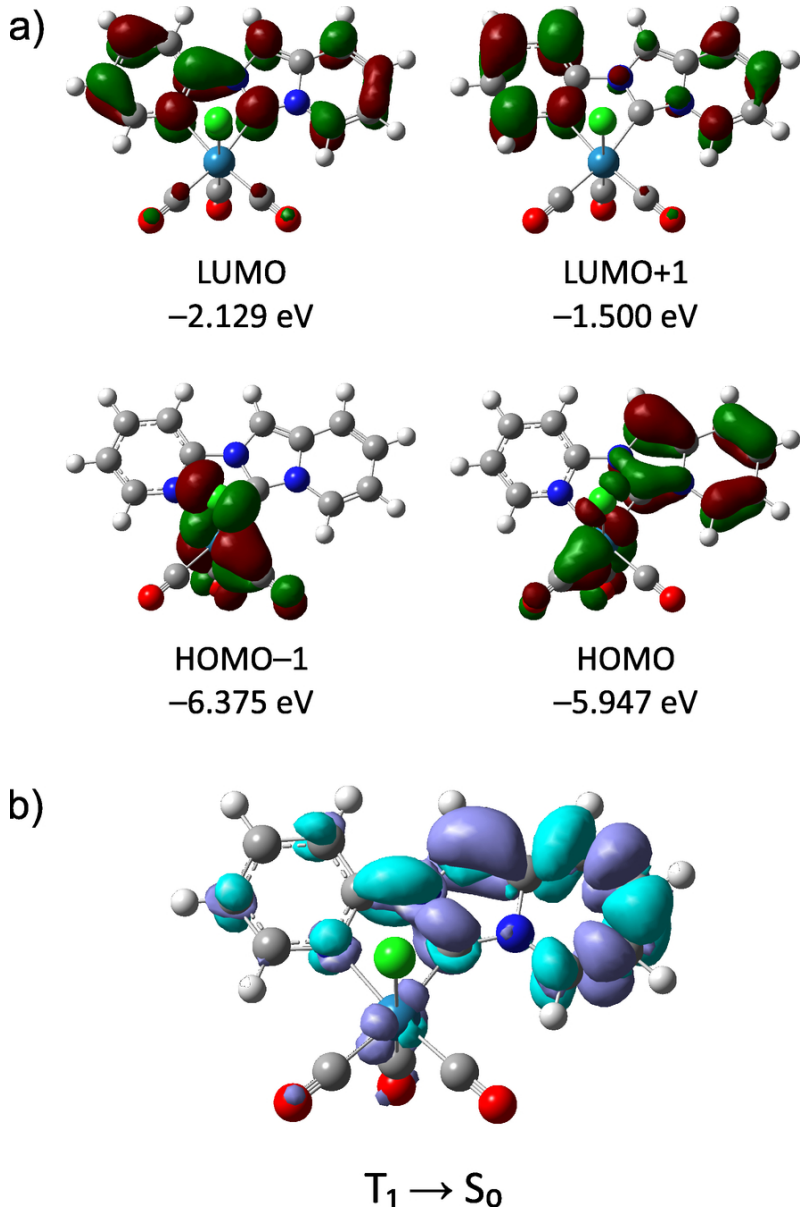

Figure 6

75x113mm (300 x 300 DPI)

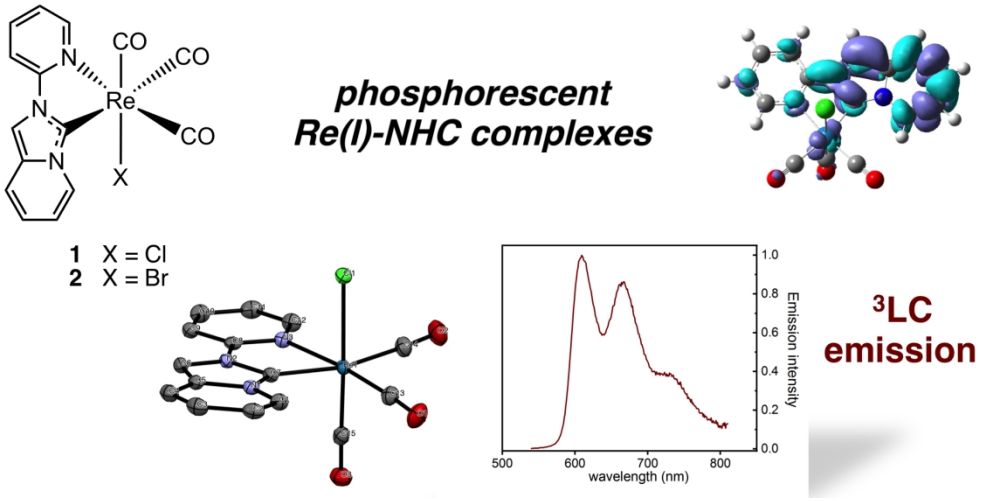

Graphical abstract

705x353mm (72 x 72 DPI)

Two novel neutral rhenium(I) tricarbonyl complexes bearing a pyridoannelated N-heterocyclic carbene are synthetized and fully characterized, which display red photoluminescence arising from a triplet excited state with ligand centered character.

ARTICLE

Electronic supplementary information

for

Red-emitting neutral rhenium(I) complexes bearing a pyridyl pyridoannelated *N*-heterocyclic carbene

Anna Bonfiglio,[a] Kevin Magra,[b] Cristina Cebrián,[b] Federico Polo,[c] Philippe C. Gros,[b,d] Pierluigi Mercandelli,[e] and Matteo Mauro*[,a]

[a] *Université de Strasbourg & CNRS, Institut de Physique et Chimie des Matériaux de Strasbourg (IPCMS), 23, rue du Loess, F-67034 Strasbourg (France), e-mail: mauro@unistra.fr*

[b] *Université de Lorraine, CNRS, L2CM, F-57000 Metz (France)*

[c] *Department of Molecular Sciences and Nanosystems, Ca' Foscari University of Venice. Via Torino 155, 30172 Venezia (Italy)*

[d] *Université de Lorraine, CNRS, L2CM, F-54000 Nancy (France)*

[e] *Dipartimento di Chimica, Università degli Studi di Milano, via Camillo Golgi 19, 20133 Milano (Italy)*

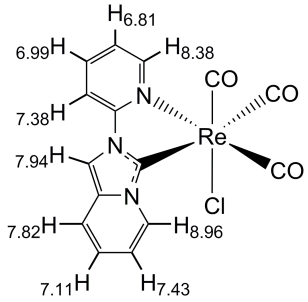

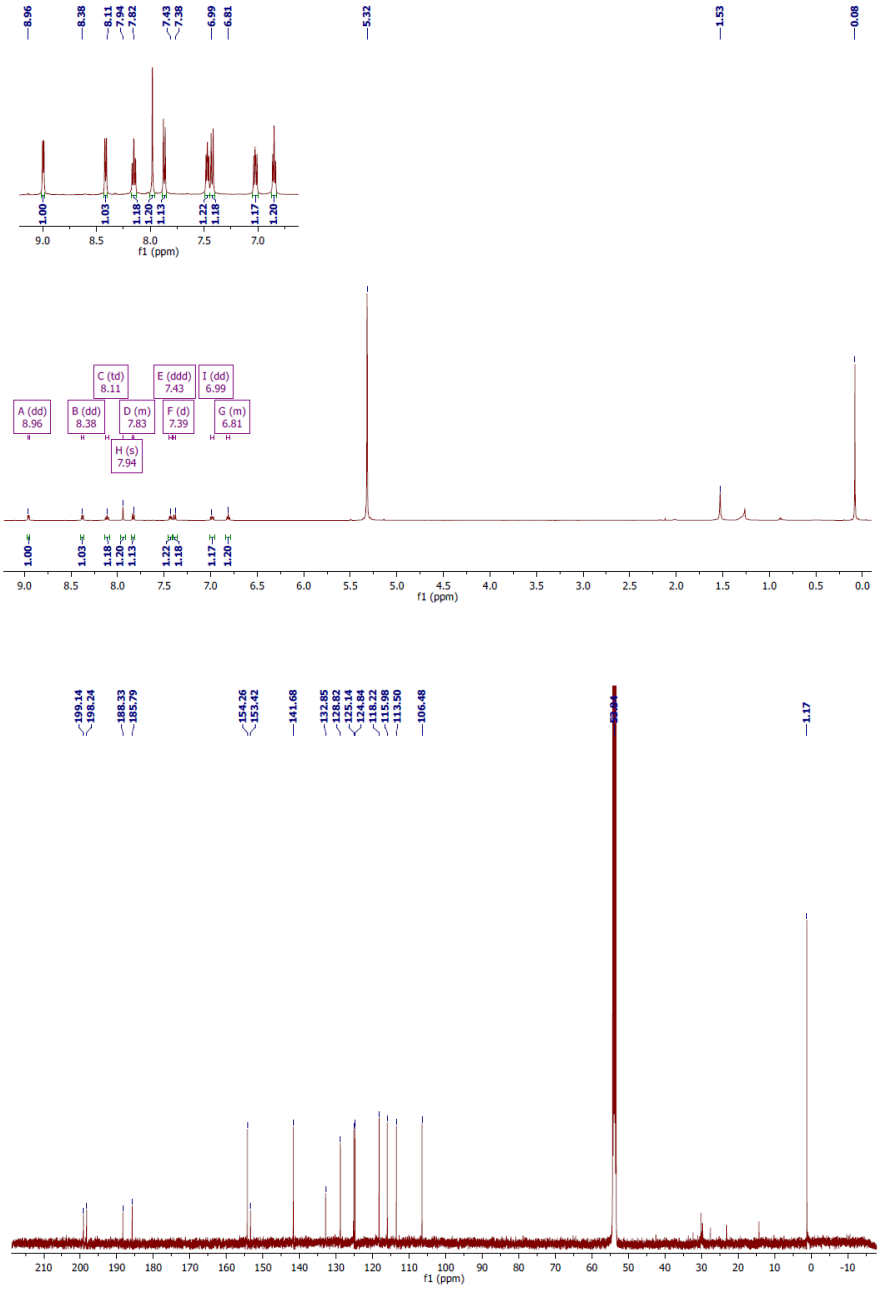

Figure S1. ^{1}H (500 MHz, *top*) and ^{13}C NMR (125 MHz, *bottom*) spectra recorded for complex **1** in CD_2Cl_2 at 298 K.

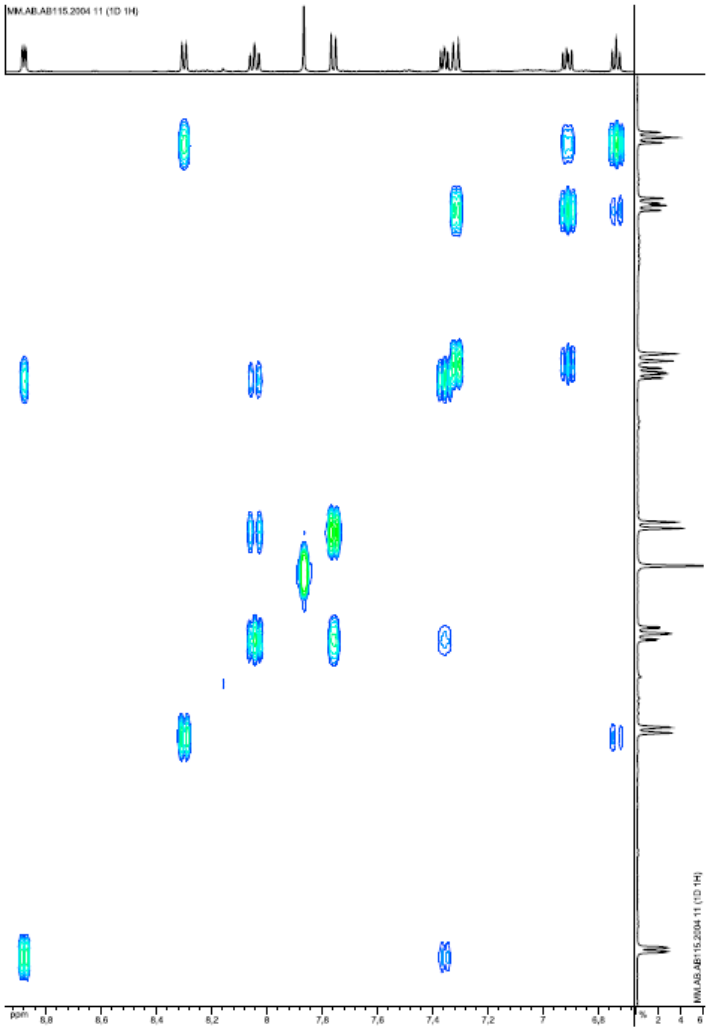

Figure S2. ^{1}H-^{1}H COSY NMR spectrum recorded for complex **1** in CD_2Cl_2 at 298 K.

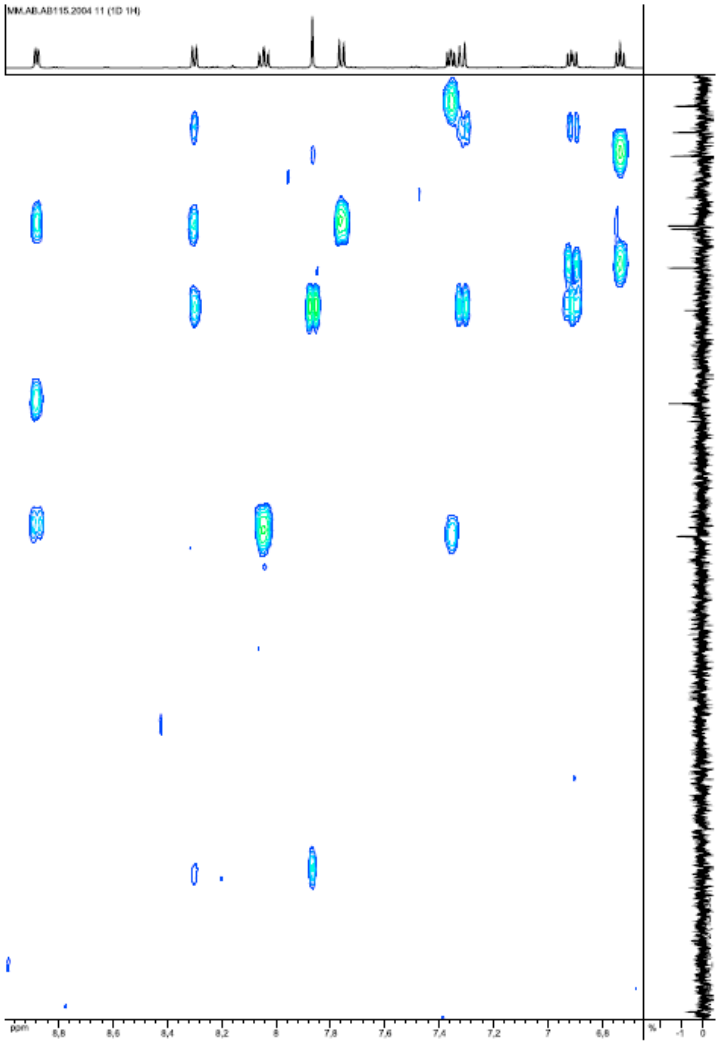

Figure S3. ^{1}H-^{13}C HMBC NMR spectrum recorded for complex **1** in CD_2Cl_2 at 298 K.

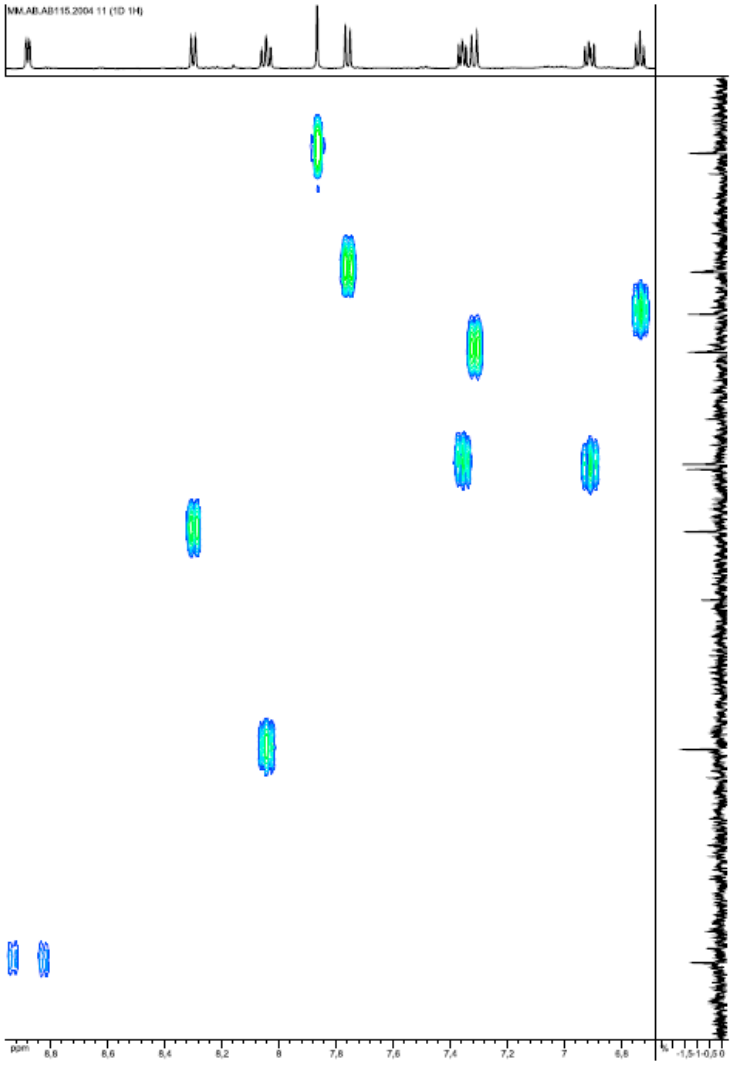

Figure S4. ^{1}H-^{13}C HSQC NMR spectrum recorded for complex **1** in CD_2Cl_2 at 298 K.

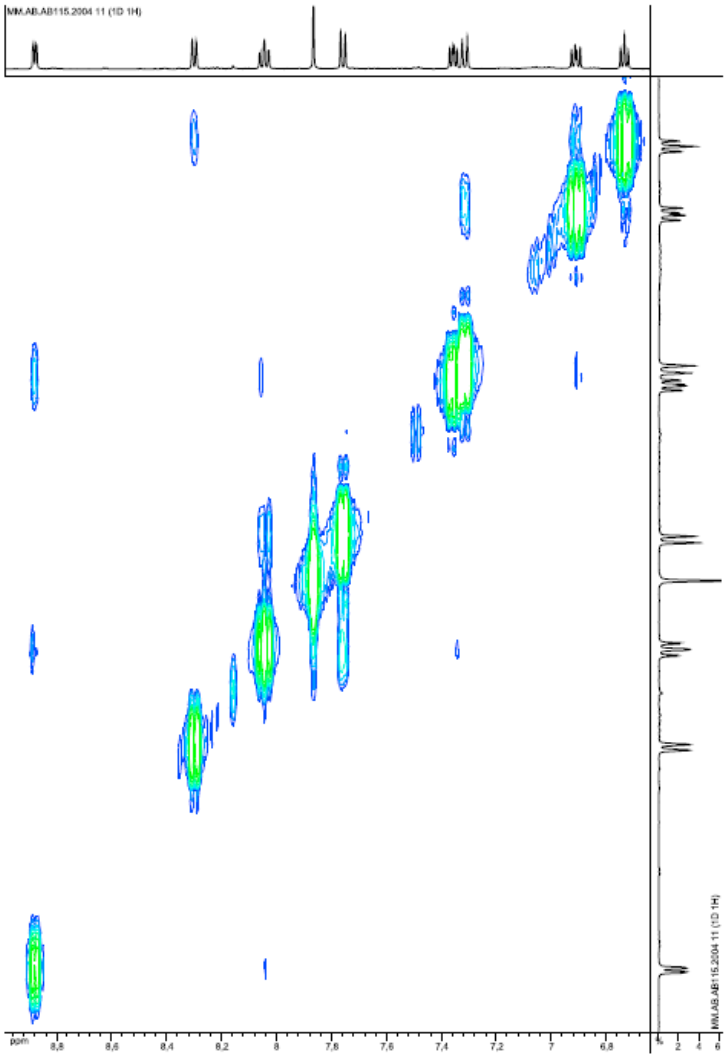

Figure S5. ^{1}H-^{1}H ROESY NMR spectrum recorded for complex **1** in CD_2Cl_2 at 298 K.

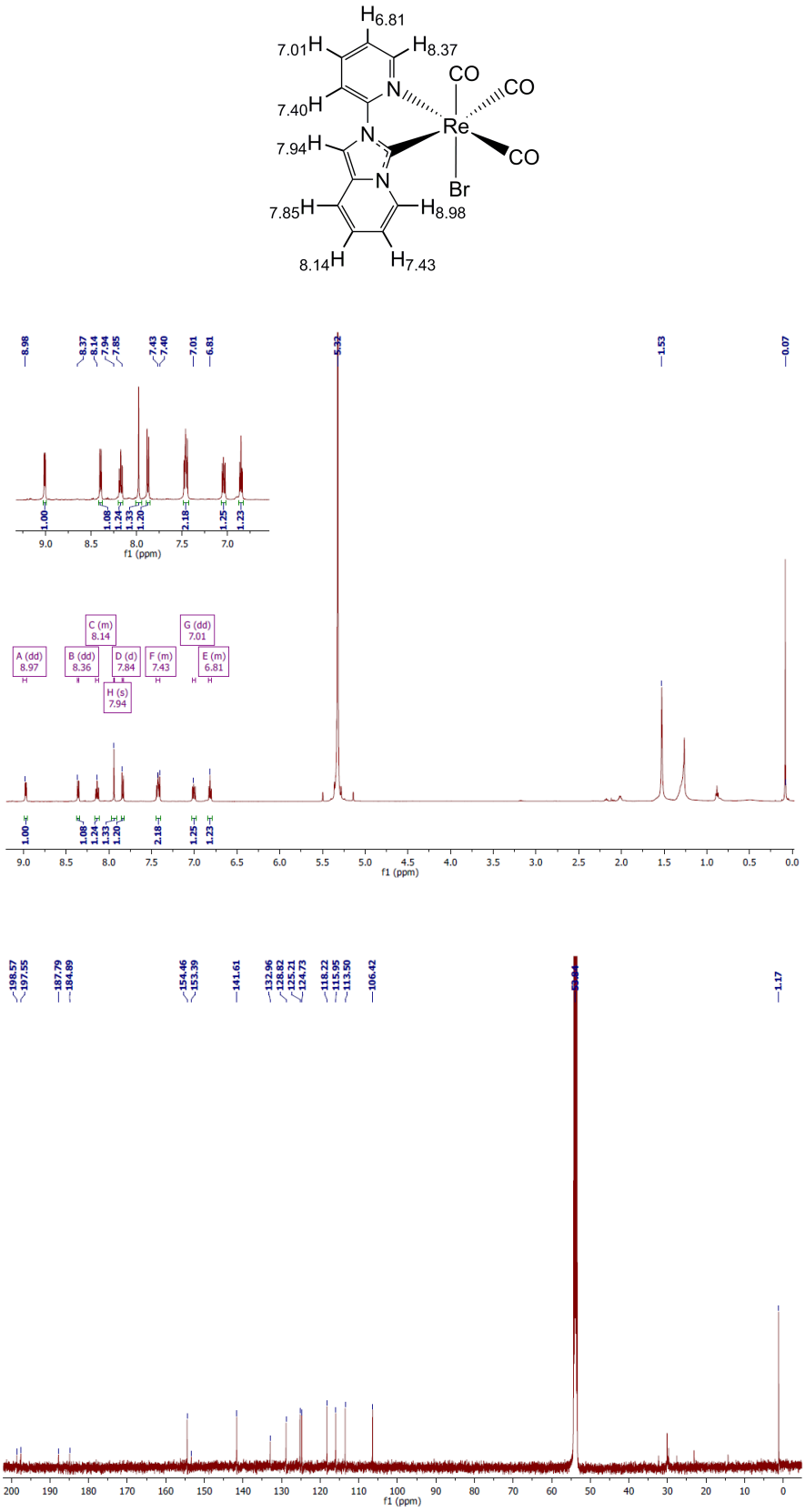

Figure S6. ^{1}H (500 MHz, *top*) and ^{13}C NMR (125 MHz, *bottom*) spectra recorded for complex **2** in CD_2Cl_2 at 298 K.

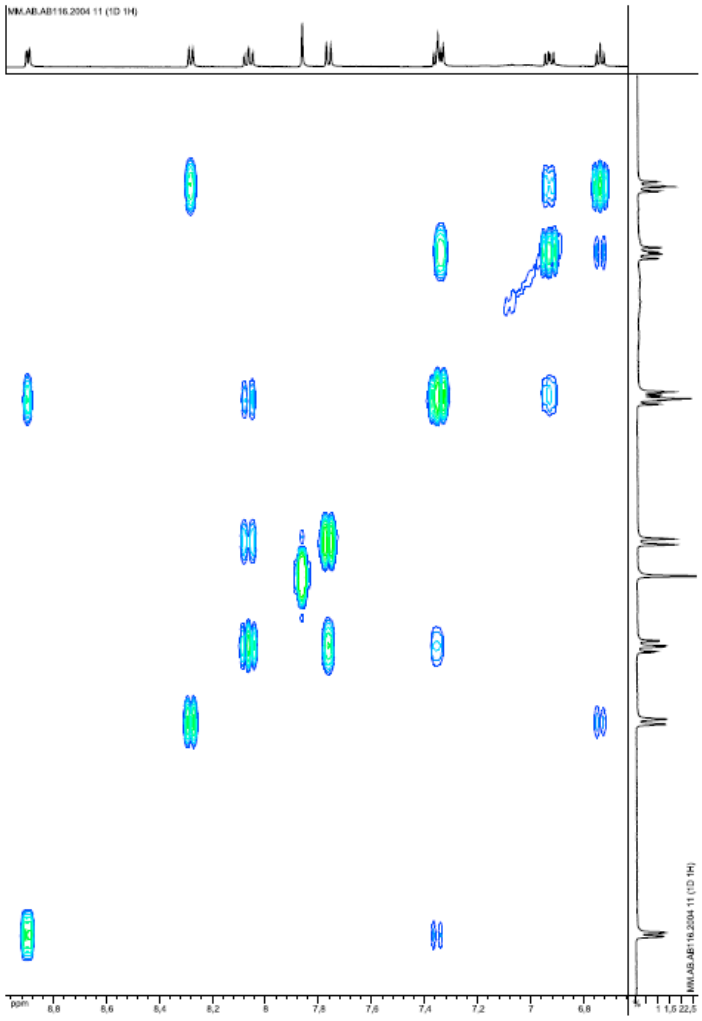

Figure S7. ^{1}H-^{1}H COSY NMR spectrum recorded for complex **2** in CD_2Cl_2 at 298 K.

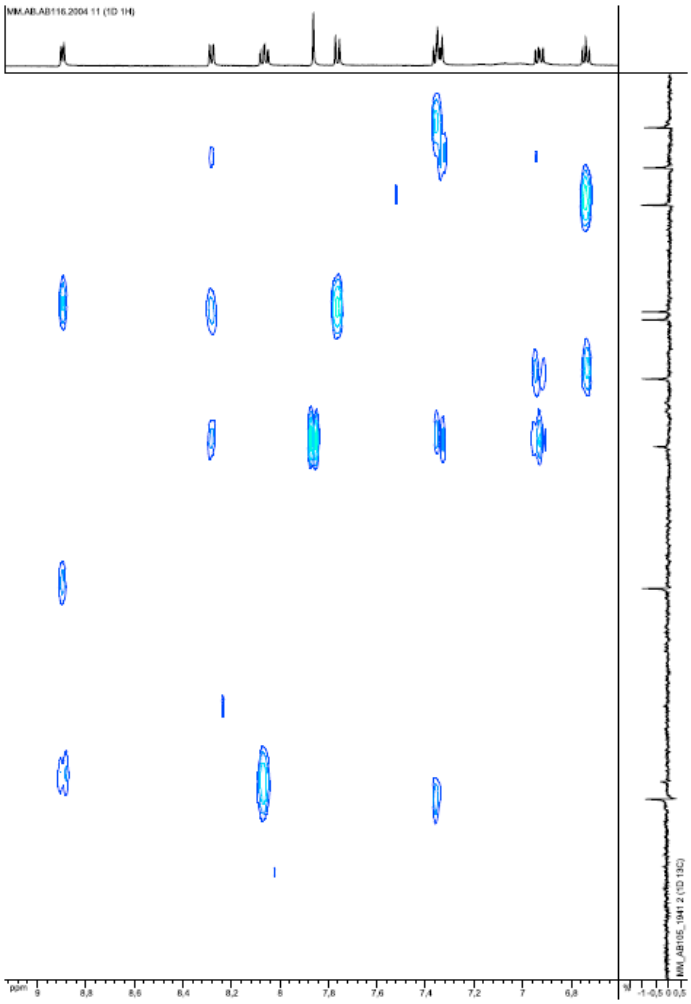

Figure S8. ^{1}H-^{13}C HMBC spectrum recorded for complex **2** in CD_2Cl_2 at 298 K.

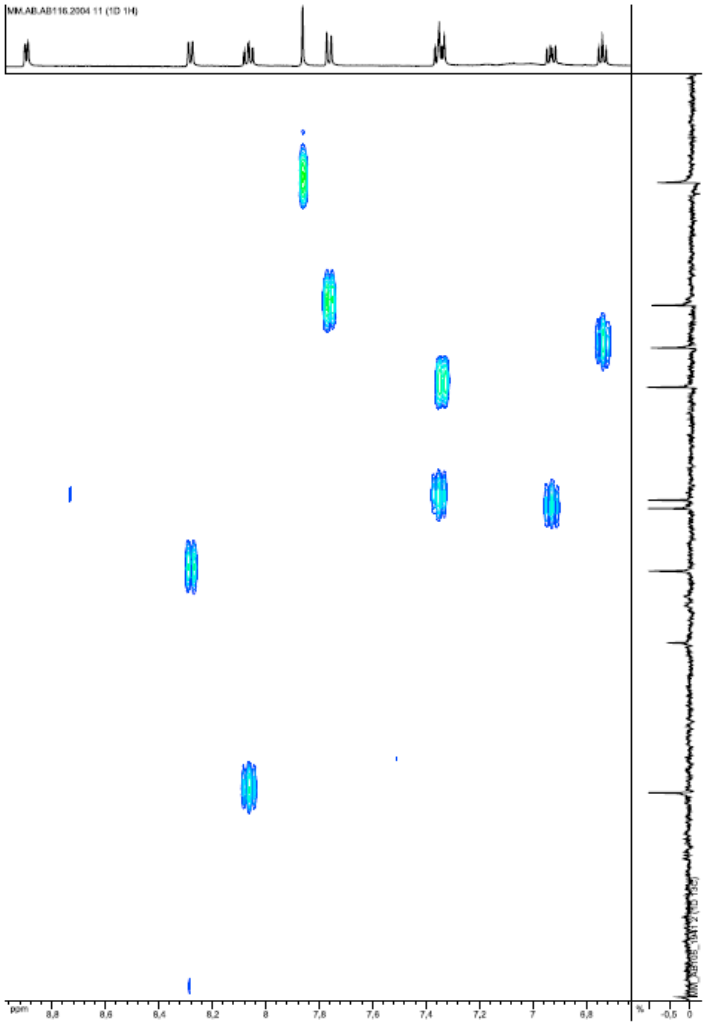

Figure S9. ^{1}H-^{13}C HSQC NMR spectrum recorded for complex **2** in CD_2Cl_2 at 298 K.

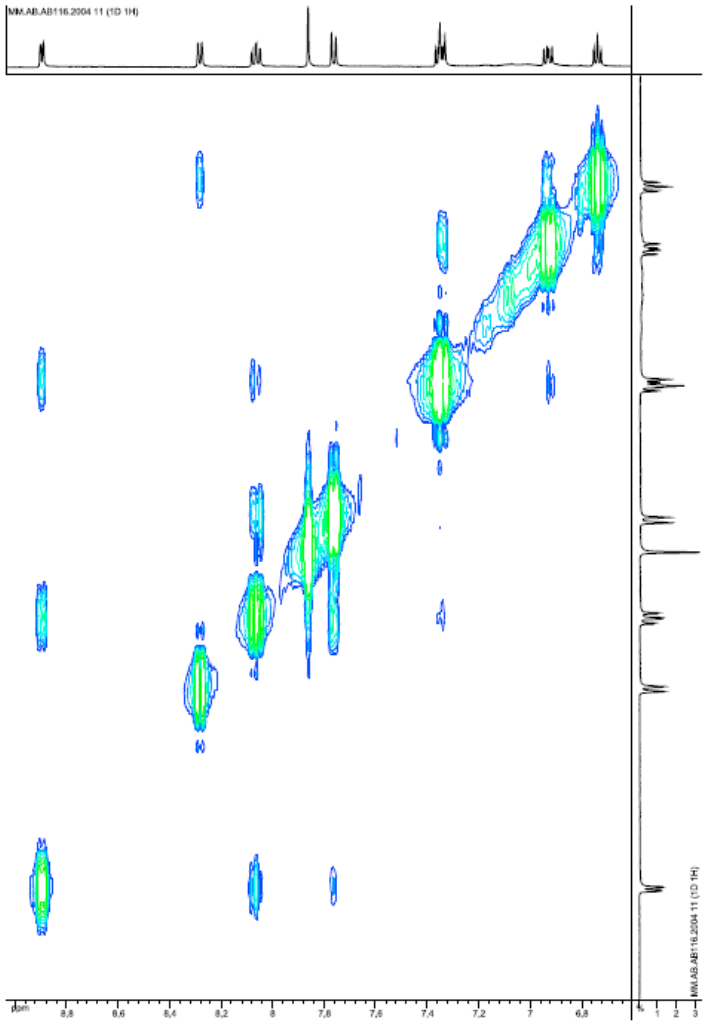

Figure S10. ^{1}H-^{1}H NOESY NMR spectrum recorded for complex **2** in CD_2Cl_2 at 298 K.

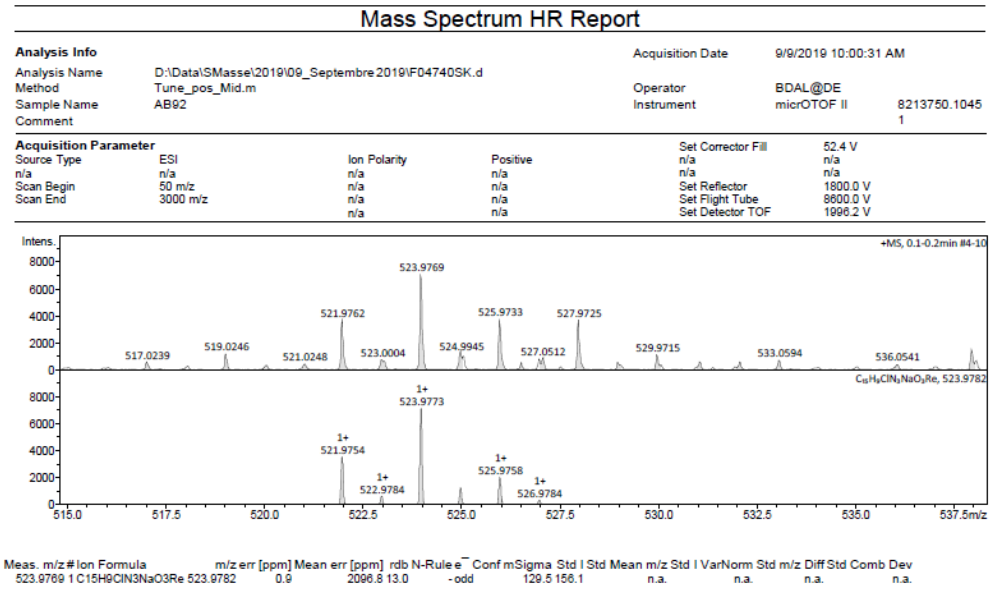

Figure S11. High-resolution ESI-MS spectrum of compound **1**.

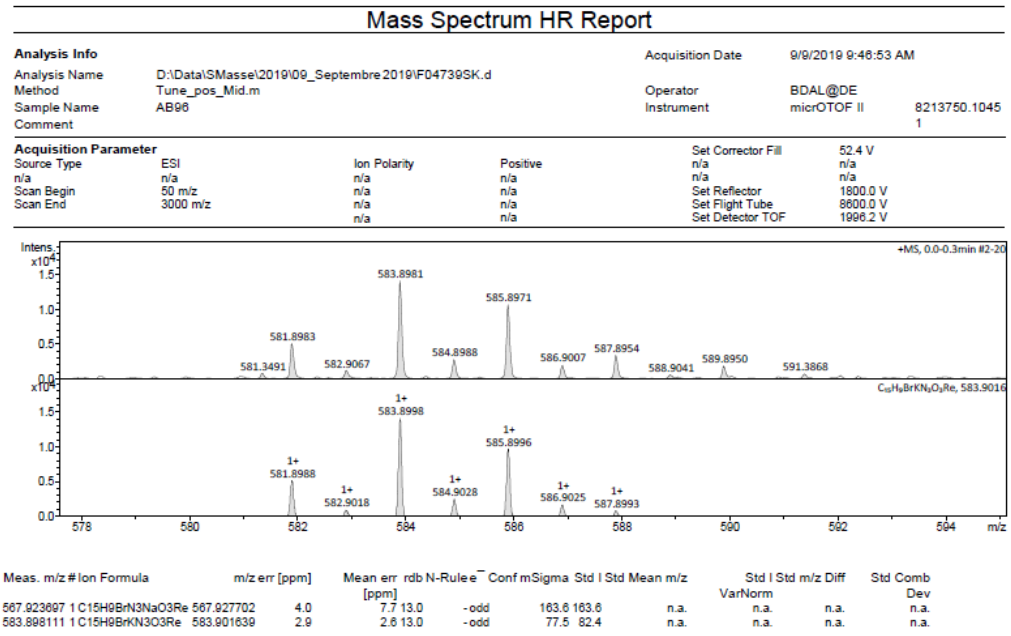

Figure S12. High-resolution ESI-MS spectrum of compound **2**.

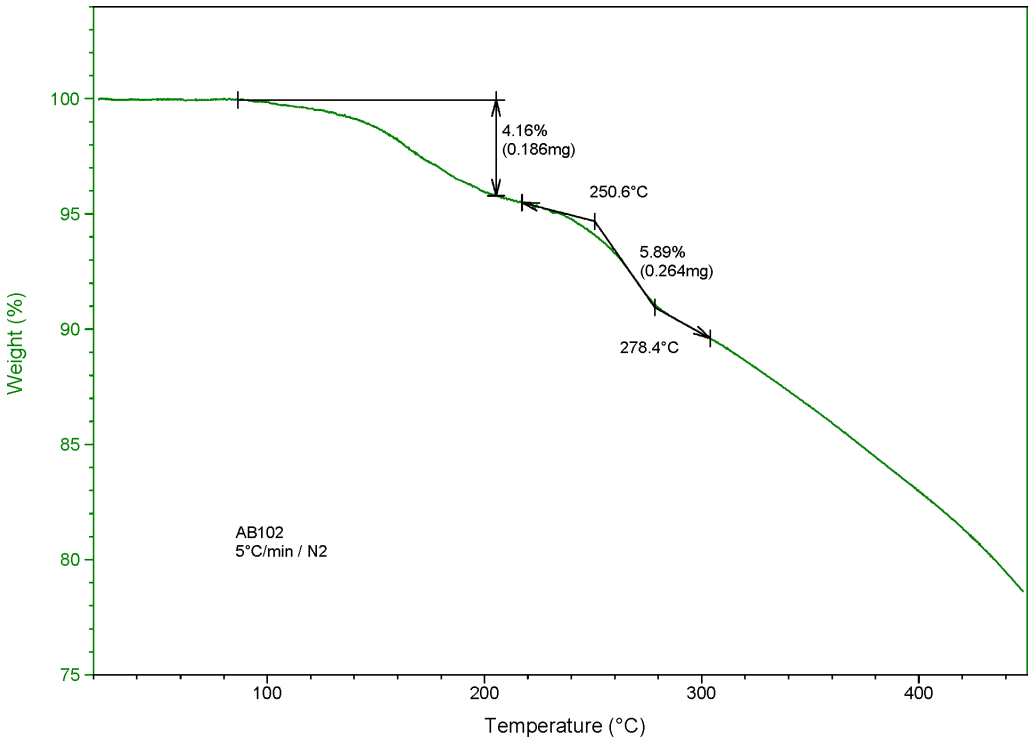

Figure S13. Thermogravimetric analysis recorded for complex **1**.

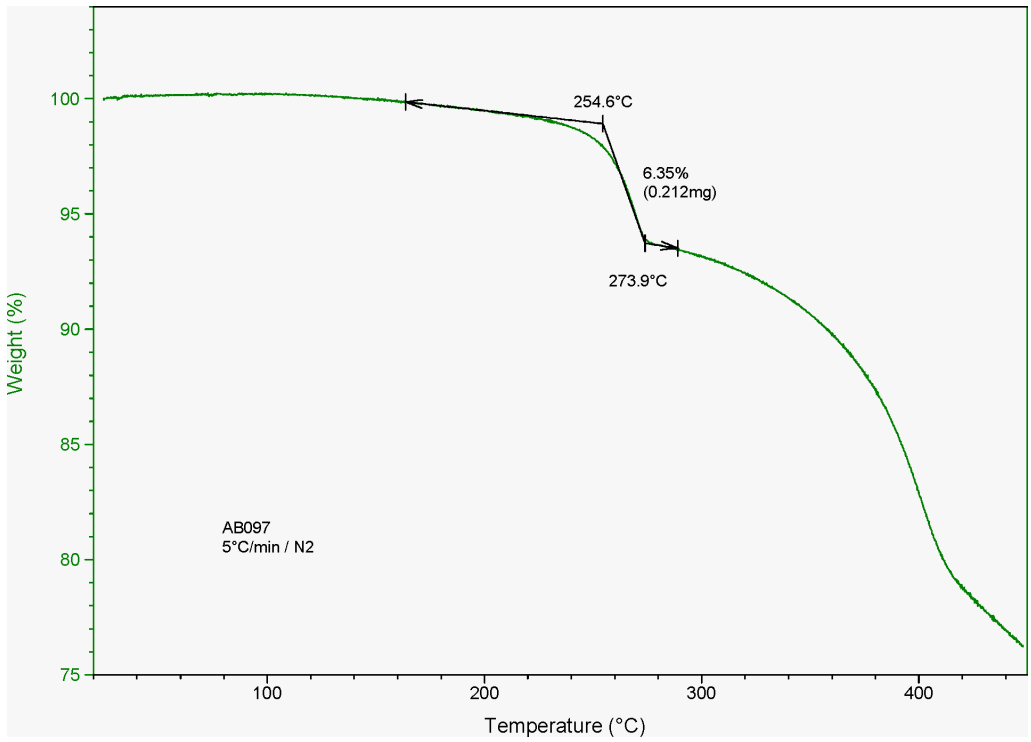

Figure S14. Thermogravimetric analysis recorded for complex **2**.

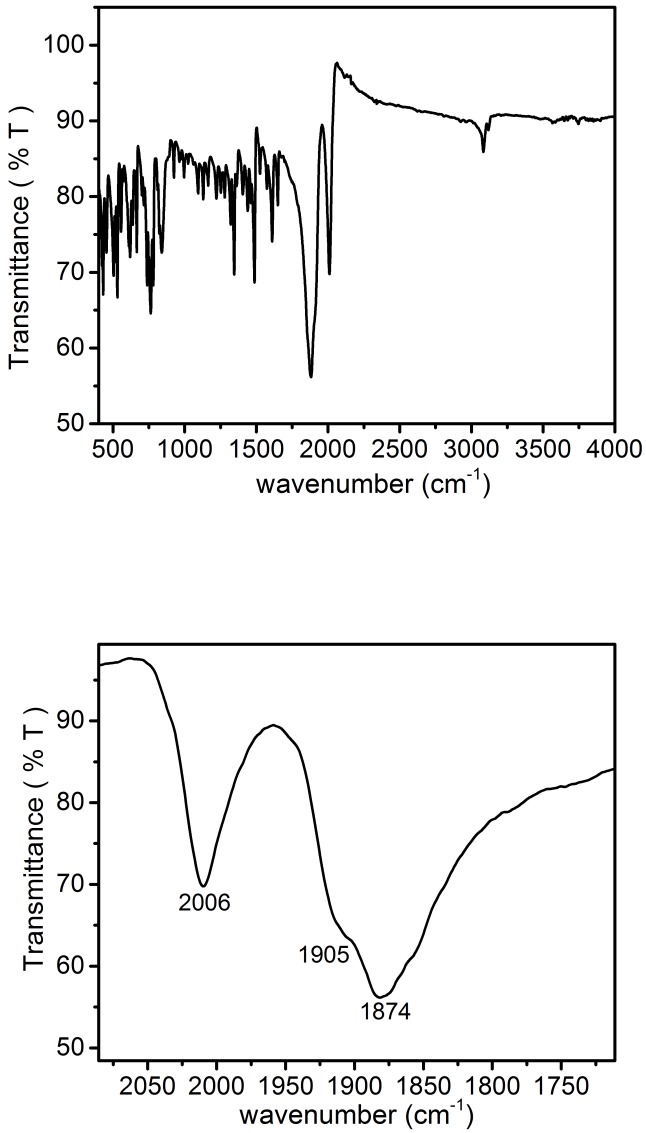

Figure S15. FT-ATR-IR spectra obtained for complex **1** in solid state as neat powder in the region 4000 – 400 cm^{-1} (*top*) and enlarged spectrum in the νC≡O region 2085 – 1711 cm^{-1} (*bottom*).

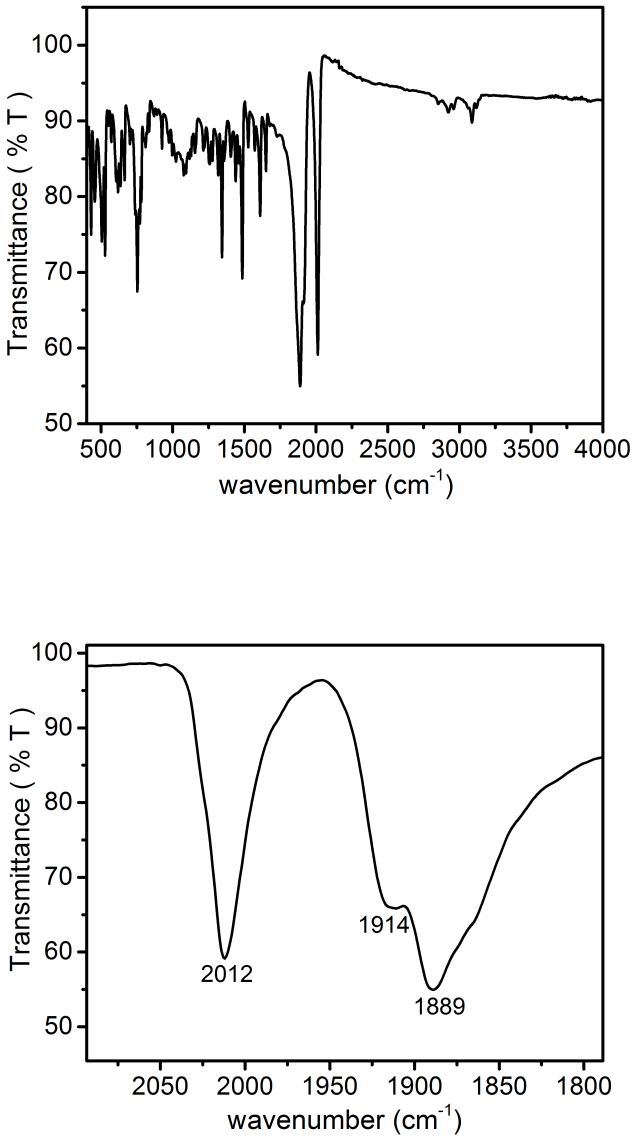

Figure S16. FT-ATR-IR spectra obtained for complex **2** in solid state as neat powder in the region 4000 – 400 cm^{-1} (*top*) and enlarged spectrum in the νC≡O region 2093 – 1788 cm^{-1} (*bottom*).

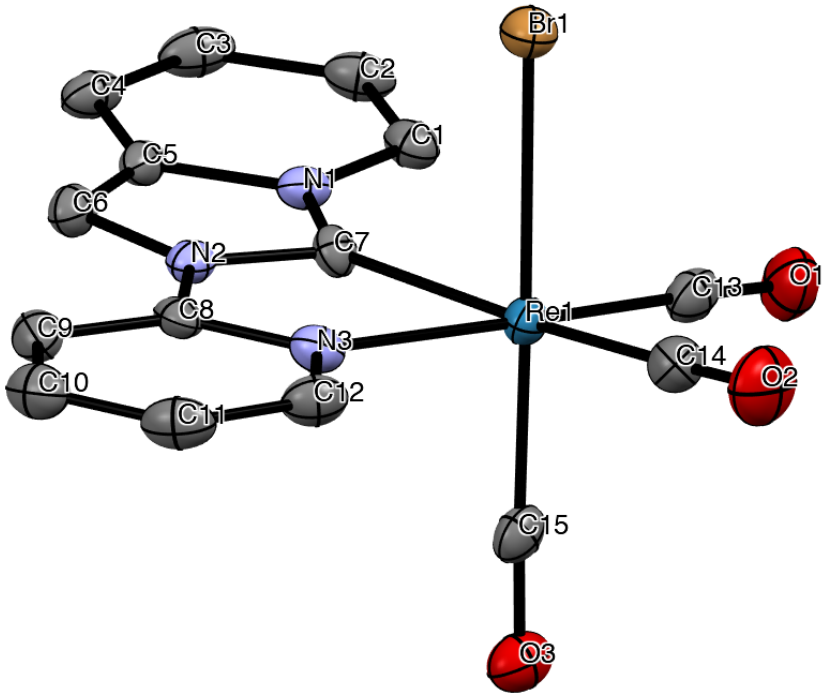

Figure S17. ORTEP diagram of compound **2** with thermal ellipsoids shown at 50% probability level obtained by single-crystal X-ray diffractometric analysis. Hydrogen atoms are omitted for clarity. Selected bond lengths (Å): Re–C(7) = 2.129(4) Å; Re–C(13) = 1.915(5) Å, Re–C(14) = 1.951(5) Å, Re–C(15) = 1.910(5) Å, Re–N(3) = 2.208(4) Å; Re–Br(1) = 2.6199(5) Å.

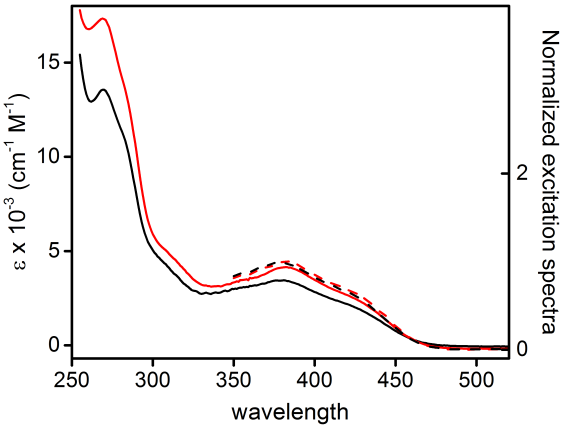

Figure S18. Electronic absorption (solid line) and normalized excitation spectra (dashed line) of complex **1** (black traces) and **2** (red traces) in degassed CH_2Cl_2 solution at a concentration of 2×10^{-5} M at room temperature. Excitation spectra were recorded setting emission at λ_{em} = 660 nm.

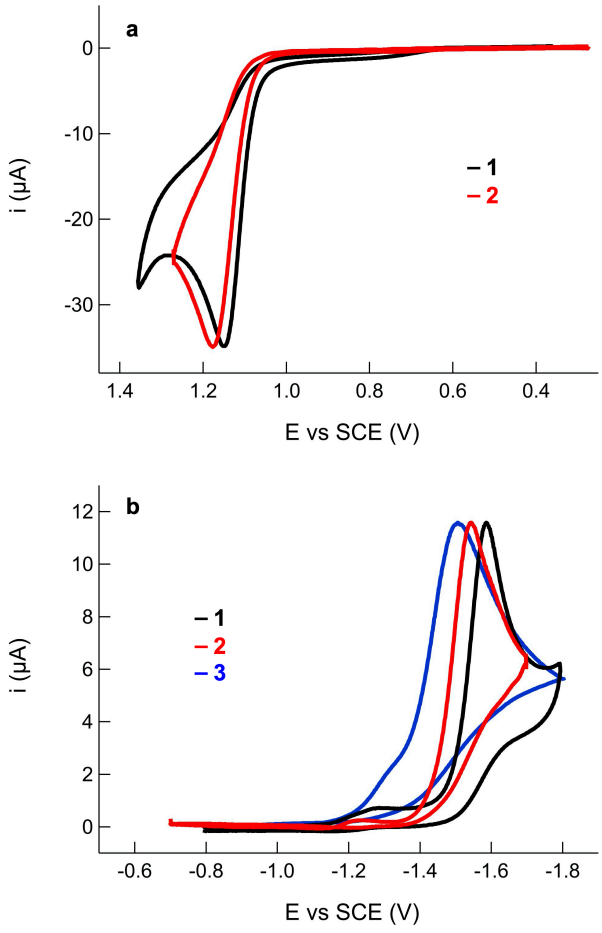

Figure S19. Blank-subtracted CVs recorded for 1 mM of compounds **1** (trace 1), compound **2** (trace 2) and ligand [pyipy]PF_6 (trace 3) in DMF/0.1 M TBAP. Scan rate: 0.1 V s^{-1}. (a) anodic and (b) cathodic processes.

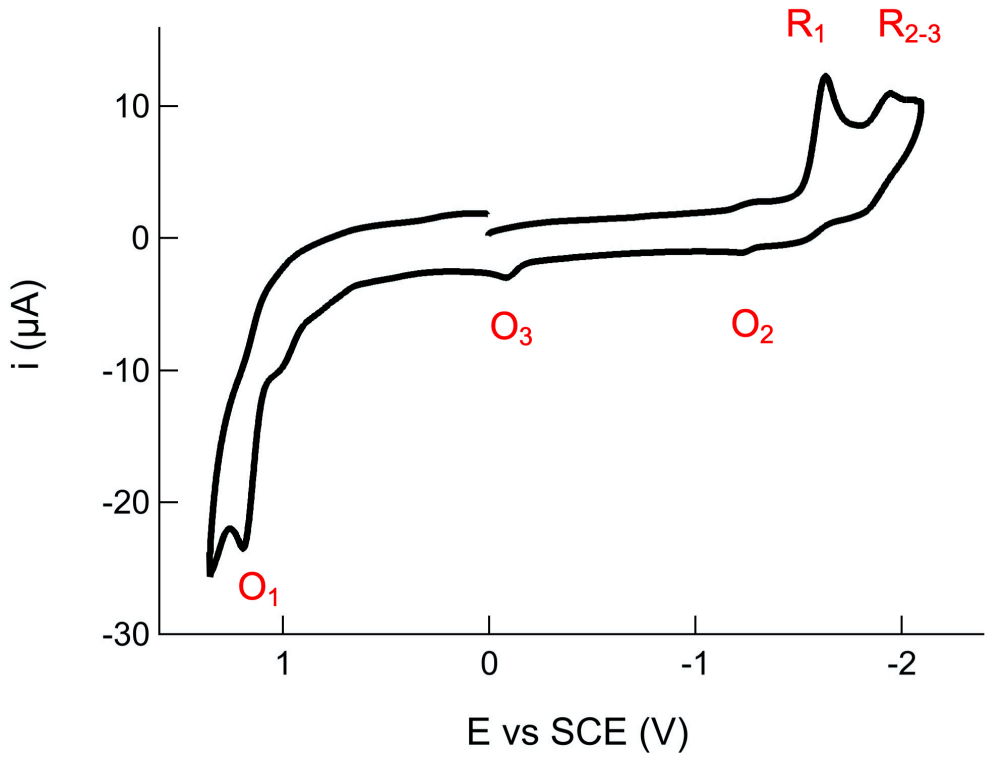

Figure S20. Full range CV of 1 mM **1** in DMF/0.1 M TBAP covering both the reduction and oxidation processes. Scan rate: 0.1 V s^{-1}.

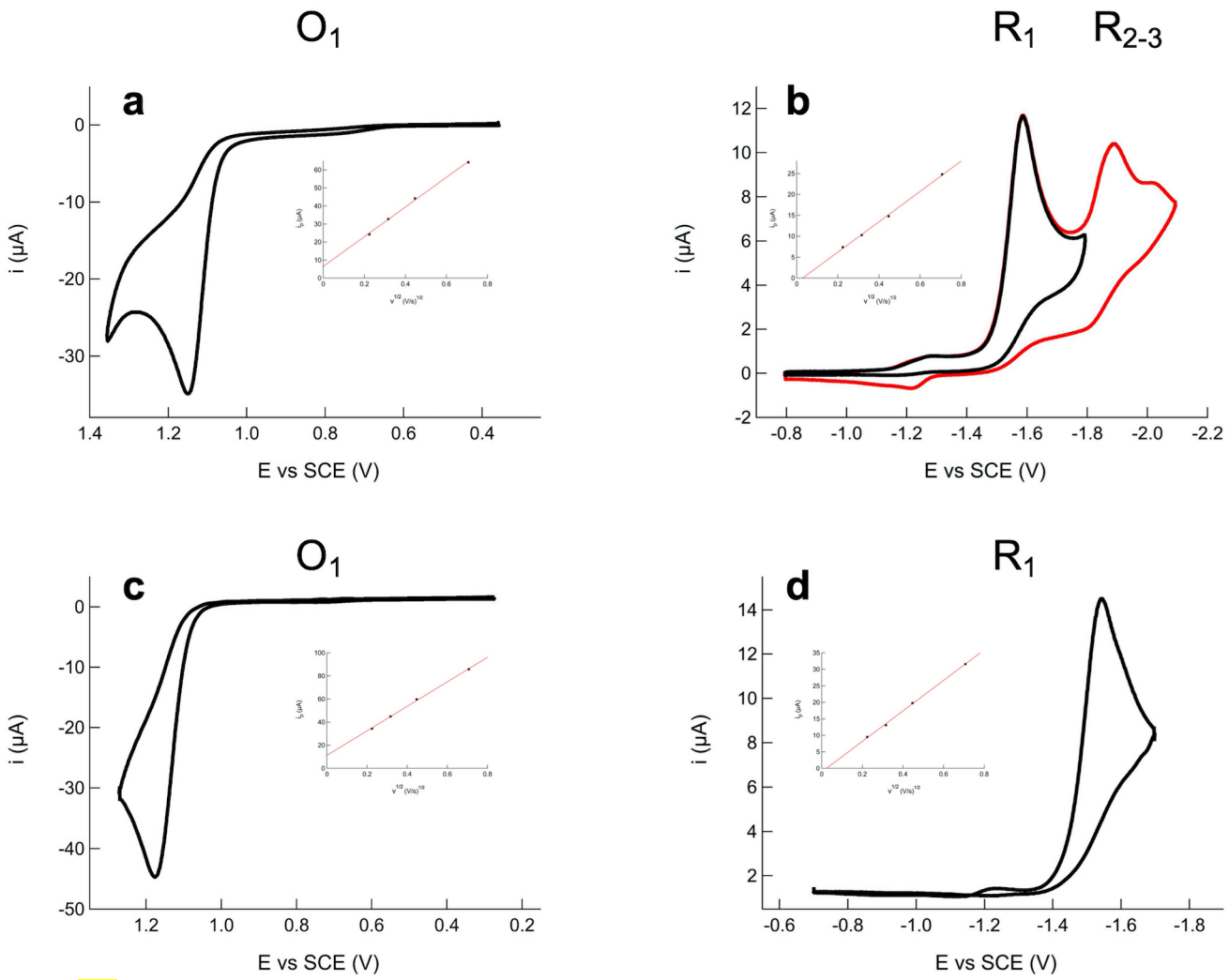

Figure S21. CVs in DMF/0.1 M TBAP showing the oxidation (a) and reduction (b) processes of 1 mM 1, and the oxidation (c) and reduction processes (d) of 1 mM **2**. The insets provide the electrochemical analyses (peak current, i_p, vs the square root of the scan rate, $v^{1/2}$) assessing the diffusion-controlled regime of the redox processes. The redox process for **1** in the negative bias covering also R_2 and R_3 is also shown (red line, b).

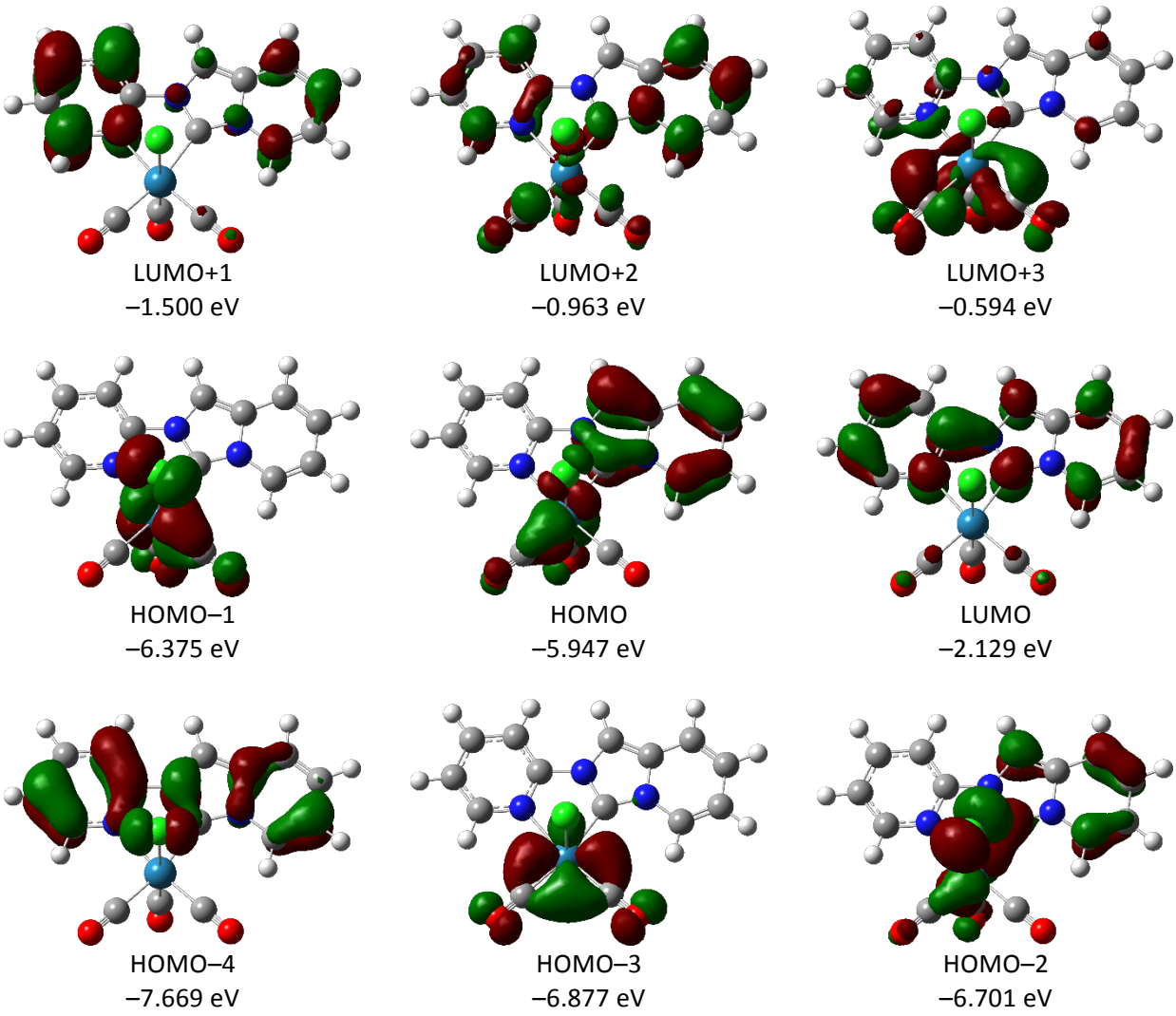

Figure S22. Isodensity surface plots and energies computed for some relevant molecular orbitals of *fac*-[Re(pyipy)$(CO)_3$Cl] (**1**).

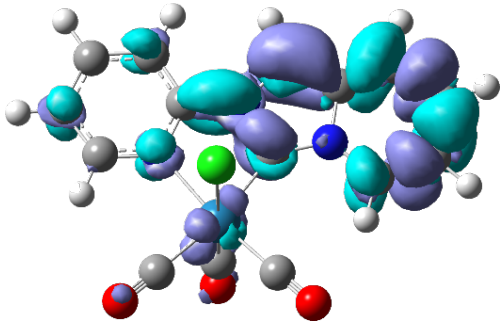

$T_1 \rightarrow S_0$
vertical transition: 1.598 eV; 776 nm
adiabatic transition: 1.982 eV; 626 nm

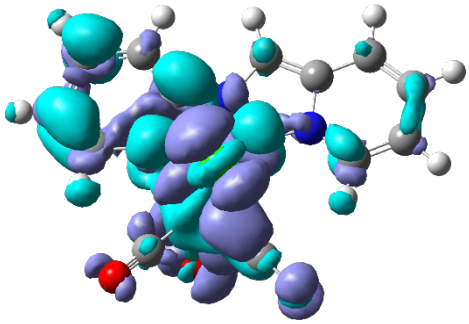

$T_2 \rightarrow S_0$
vertical transition: 2.344 eV; 529 nm
adiabatic transition: 2.831 eV; 438 nm

Figure S23. Electronic density difference maps computed (at the optimized geometry of the corresponding triplet) for the vertical transition $T_1 \rightarrow S_0$ and $T_2 \rightarrow S_0$ of *fac*-[Re(pyipy)(CO)$_3$Cl] (**1**). Energy computed for the corresponding adiabatic transition is also reported. The difference in energy between the T_1 and T_2 minima is 31.210 mE_h (0.849 eV; 6850 cm^{-1}).

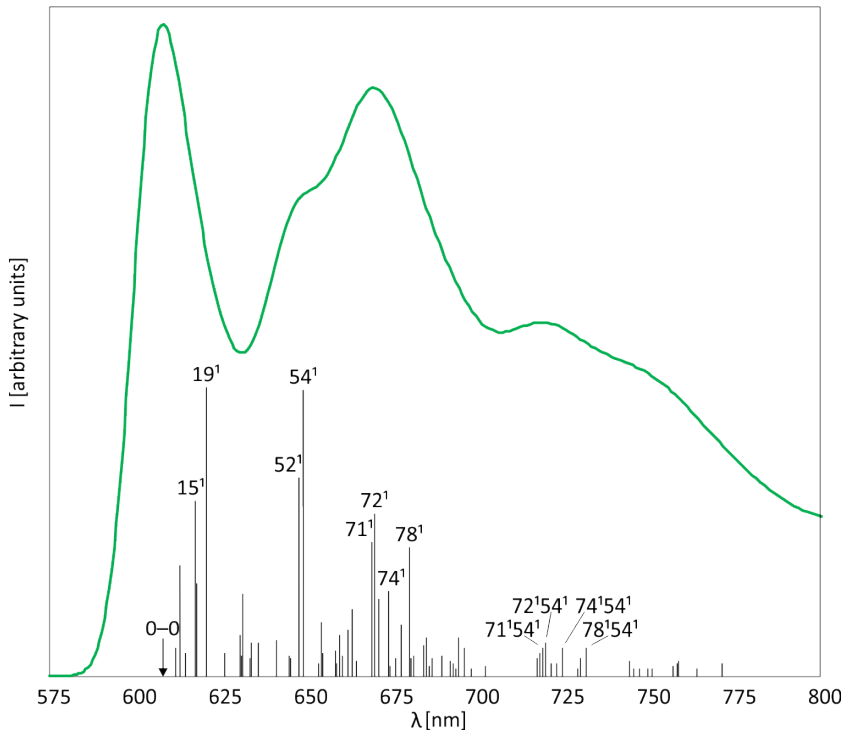

Figure S24. Assignment of the main bands of the computed emission spectrum of the $T_1 \rightarrow S_0$ electronic transition of *fac*-[Re(pyipy)(CO)$_3$Cl] (**1**). The solid line reports the harmonic spectrum calculated within the Franck-Condon approximation (half-width at half-maximum set to 220 cm^{-1}) and the sticks are labelled as ν^x where ν is the ground state normal mode and x its quantum number.

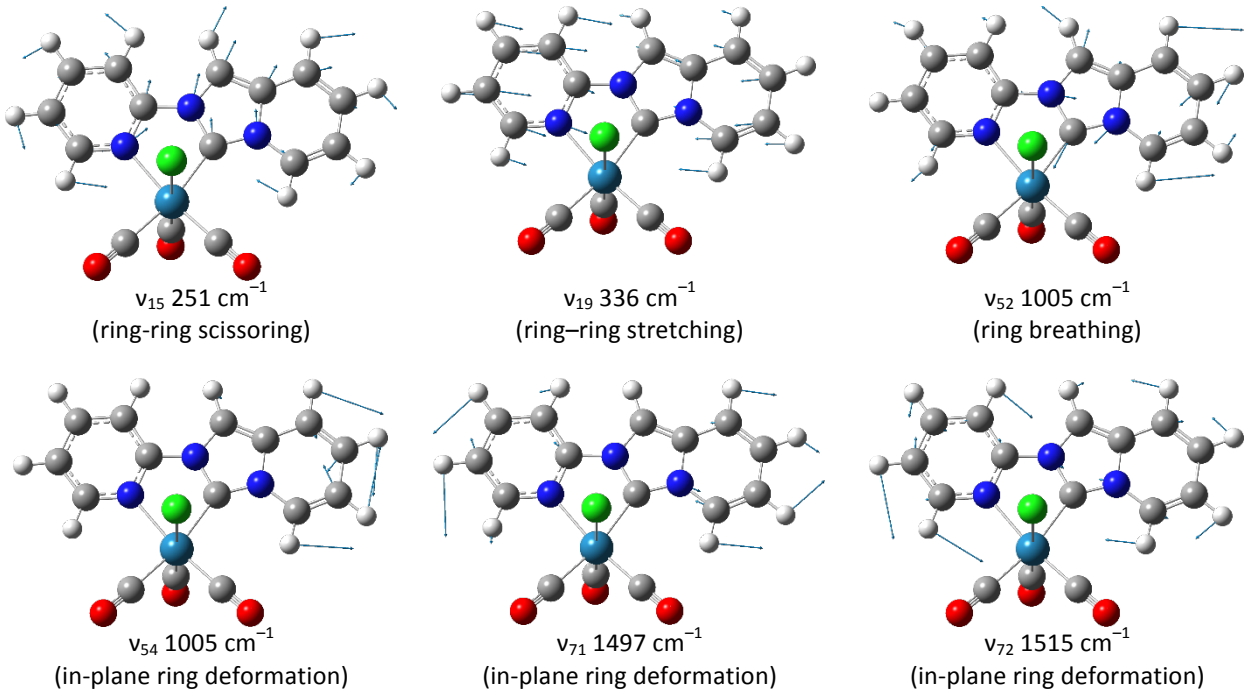

Figure S25. Some relevant normal modes computed for the ground state of *fac*-[Re(pyipy)(CO)$_3$Cl] (**1**).

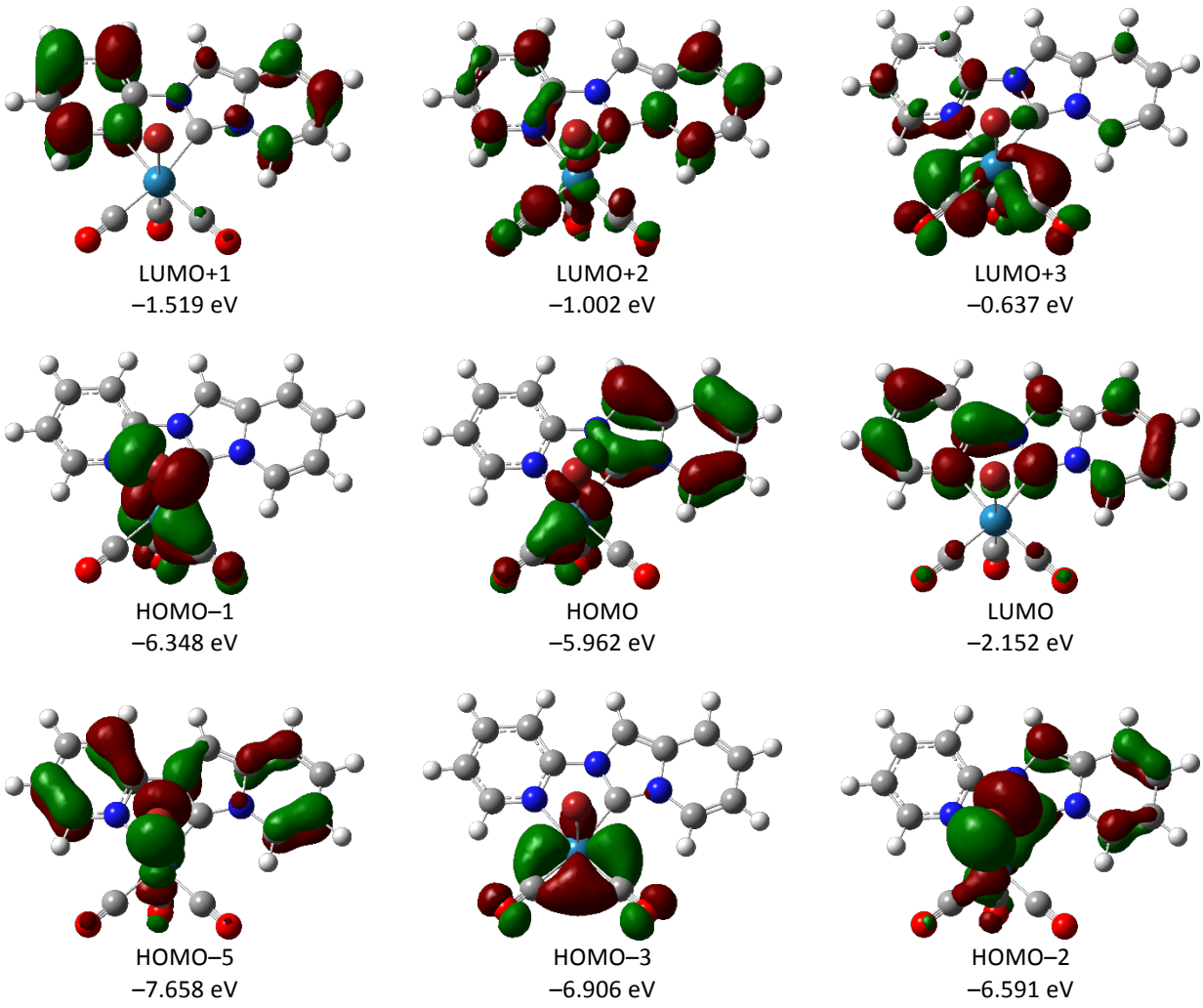

Figure S26. Isodensity surface plots and energies computed for some relevant molecular orbitals of *fac*-[Re(pyipy)$(CO)_3$Br] (**2**).

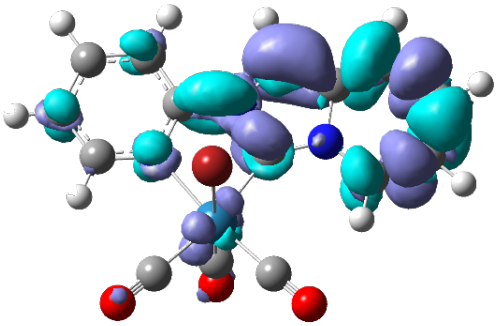

$T_1 \rightarrow S_0$
vertical transition: 1.598 eV; 776 nm
adiabatic transition: 1.979 eV; 626 nm

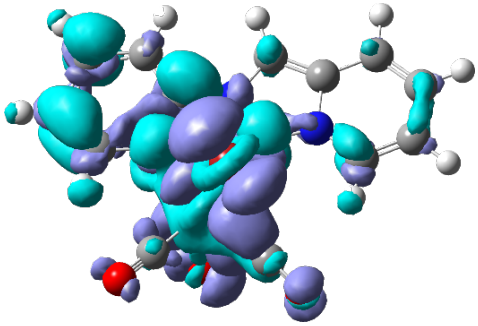

$T_2 \rightarrow S_0$
vertical transition: 2.362 eV; 525 nm
adiabatic transition: 2.825 eV; 439 nm

Figure S27. Electronic density difference maps computed (at the optimized geometry of the corresponding triplet) for the vertical transition $T_1 \rightarrow S_0$ and $T_2 \rightarrow S_0$ of *fac*-[Re(pypi)$(CO)_3$Br] (**2**). Energy computed for the corresponding adiabatic transition is also reported. The difference in energy between the T_1 and T_2 minima is 31.088 mE_h (0.846 eV; 6823 cm^{-1}). Cyan and violet indicates a decrease and increase in electron density, respectively.

Table S1. Crystal data and structure refinement for compound **1**.

Identification code	CCDC 1973530
Empirical formula	C15 H9 Cl N3 O3 Re
Formula weight	500.90
Temperature	120(2) K
Wavelength	0.71073 Å
Crystal system, space group	Triclinic, P -1
Unit cell dimensions	*a* = 6.6594(2) Å α = 89.3060(10)° *b* = 10.8376(4) Å β = 77.6610(10)° *c* = 11.1557(4) Å γ = 72.2660(10)°
Volume	747.94(4) Å^3
Z, Calculated density	2, 2.224 Mg/m^3
Absorption coefficient	8.319 mm^{-1}
F(000)	472
Crystal size	0.200 x 0.150 x 0.120 mm
Theta range for data collection	1.976 to 30.076 deg.
Limiting indices	-9<=*h*<=9, -15<=*k*<=13, -15<=*l*<=15
Reflections collected / unique	54563 / 4399 [R(int) = 0.0367]
Completeness to theta = 25.242	99.9%
Absorption correction	Semi-empirical from equivalents
Max. and min. transmission	0.7460 and 0.6059
Refinement method	Full-matrix least-squares on F^2
Data / restraints / parameters	4399 / 0 / 208
Goodness-of-fit on F^2	1.106
Final R indices [I>2σ(I)]	*R*1 = 0.0152, wR2 = 0.0302
R indices (all data)	*R*1 = 0.0163, wR2 = 0.0305
Extinction coefficient	n/a
Largest diff. peak and hole	1.616 and -0.985 *e* Å^{-3}

Table S2. Geometrical parameters obtained for compound **1** by means of X-ray crystallographic analysis.

Bond lengths [A]

C(1)-C(2)	1.347(3)
C(1)-N(1)	1.396(3)
C(1)-H(1)	0.9500
C(2)-C(3)	1.437(3)
C(2)-H(2)	0.9500
C(3)-C(4)	1.353(3)
C(3)-H(3)	0.9500
C(4)-C(5)	1.425(3)
C(4)-H(4)	0.9500
C(5)-C(6)	1.365(3)
C(5)-N(1)	1.415(3)
C(6)-N(2)	1.387(2)
C(6)-H(6)	0.9500
C(7)-N(1)	1.359(3)
C(7)-N(2)	1.370(3)
C(7)-Re(1)	2.126(2)
C(8)-N(3)	1.342(3)
C(8)-C(9)	1.386(3)
C(8)-N(2)	1.411(3)
C(9)-C(10)	1.384(3)
C(9)-H(9)	0.9500
C(10)-C(11)	1.389(3)
C(10)-H(10)	0.9500
C(11)-C(12)	1.378(3)
C(11)-H(11)	0.9500
C(12)-N(3)	1.358(3)
C(12)-H(12)	0.9500
C(13)-O(1)	1.156(3)
C(13)-Re(1)	1.913(2)
C(14)-O(2)	1.145(3)
C(14)-Re(1)	1.957(2)
C(15)-O(3)	1.147(3)
C(15)-Re(1)	1.914(2)
N(3)-Re(1)	2.2085(17)
Cl(1)-Re(1)	2.5049(5)

Bond angles [°]

C(2)-C(1)-N(1)	119.1(2)
C(2)-C(1)-H(1)	120.5
N(1)-C(1)-H(1)	120.5
C(1)-C(2)-C(3)	121.3(2)
C(1)-C(2)-H(2)	119.4
C(3)-C(2)-H(2)	119.4
C(4)-C(3)-C(2)	120.5(2)
C(4)-C(3)-H(3)	119.8
C(2)-C(3)-H(3)	119.8
C(3)-C(4)-C(5)	119.3(2)
C(3)-C(4)-H(4)	120.3
C(5)-C(4)-H(4)	120.3
C(6)-C(5)-N(1)	106.30(17)
C(6)-C(5)-C(4)	134.8(2)
N(1)-C(5)-C(4)	118.85(19)
C(5)-C(6)-N(2)	105.53(17)

C(5)-C(6)-H(6)	127.2
N(2)-C(6)-H(6)	127.2
N(1)-C(7)-N(2)	102.88(16)
N(1)-C(7)-Re(1)	140.64(15)
N(2)-C(7)-Re(1)	116.36(14)
N(3)-C(8)-C(9)	124.18(19)
N(3)-C(8)-N(2)	113.63(17)
C(9)-C(8)-N(2)	122.18(18)
C(10)-C(9)-C(8)	117.66(19)
C(10)-C(9)-H(9)	121.2
C(8)-C(9)-H(9)	121.2
C(9)-C(10)-C(11)	119.5(2)
C(9)-C(10)-H(10)	120.2
C(11)-C(10)-H(10)	120.2
C(12)-C(11)-C(10)	118.9(2)
C(12)-C(11)-H(11)	120.5
C(10)-C(11)-H(11)	120.5
N(3)-C(12)-C(11)	122.7(2)
N(3)-C(12)-H(12)	118.6
C(11)-C(12)-H(12)	118.6
O(1)-C(13)-Re(1)	176.2(2)
O(2)-C(14)-Re(1)	177.1(2)
O(3)-C(15)-Re(1)	178.6(2)
C(7)-N(1)-C(1)	127.11(18)
C(7)-N(1)-C(5)	111.86(17)
C(1)-N(1)-C(5)	120.99(17)
C(7)-N(2)-C(6)	113.41(17)
C(7)-N(2)-C(8)	118.68(17)
C(6)-N(2)-C(8)	127.90(17)
C(8)-N(3)-C(12)	116.99(18)
C(8)-N(3)-Re(1)	117.26(13)
C(12)-N(3)-Re(1)	125.64(14)
C(13)-Re(1)-C(15)	87.28(9)
C(13)-Re(1)-C(14)	89.70(9)
C(15)-Re(1)-C(14)	91.94(9)
C(13)-Re(1)-C(7)	100.48(9)
C(15)-Re(1)-C(7)	94.99(8)
C(14)-Re(1)-C(7)	167.92(9)
C(13)-Re(1)-N(3)	173.71(8)
C(15)-Re(1)-N(3)	90.34(8)
C(14)-Re(1)-N(3)	96.20(8)
C(7)-Re(1)-N(3)	73.92(7)
C(13)-Re(1)-Cl(1)	95.95(7)
C(15)-Re(1)-Cl(1)	176.71(7)
C(14)-Re(1)-Cl(1)	87.46(7)
C(7)-Re(1)-Cl(1)	85.05(5)
N(3)-Re(1)-Cl(1)	86.51(5)

Table S3. Crystal data and structure refinement for compound **2**.

Identification code	CCDC 1980932
Empirical formula	C15 H9 Br N3 O3 Re
Formula weight	545.36
Temperature	120(2) K
Wavelength	0.71073 Å
Crystal system, space group	Triclinic, P -1
Unit cell dimensions	*a* = 6.7338(3) Å α = 88.7910(10)° *b* = 10.8986(4) Å β = 76.4800(10)° *c* = 11.3120(5) Å γ = 72.1440(10)°
Volume	767.14(6) Å^3
Z, Calculated density	2, 2.361 Mg/m^3
Absorption coefficient	10.542 mm^{-1}
F(000)	508
Crystal size	0.180 x 0.150 x 0.120 mm
Theta range for data collection	1.966 to 29.168 deg.
Limiting indices	-9<=h<=9, -14<=k<=14, -15<=l<=15
Reflections collected / unique	54752 / 4137 [R(int) = 0.0597]
Completeness to theta = 25.242	100.0 %
Absorption correction	Semi-empirical from equivalents
Max. and min. transmission	0.7458 and 0.5741
Refinement method	Full-matrix least-squares on F^2
Data / restraints / parameters	4137 / 0 / 208
Goodness-of-fit on F^2	1.109
Final R indices [I>2σ(I)]	*R*1 = 0.0295, w*R*2 = 0.0621
R indices (all data)	*R*1 = 0.0342, w*R*2 = 0.0649
Extinction coefficient	n/a
Largest diff. peak and hole	3.362 and -1.941 *e* Å^{-3}

Table S4. Geometrical parameters obtained for compound **2** by means of X-ray crystallographic analysis.

Bond lengths [A]

C(1)-C(2)	1.347(7)
C(1)-N(1)	1.396(6)
C(1)-H(1)	0.9500
C(2)-C(3)	1.440(8)
C(2)-H(2)	0.9500
C(3)-C(4)	1.339(8)
C(3)-H(3)	0.9500
C(4)-C(5)	1.428(7)
C(4)-H(4)	0.9500
C(5)-C(6)	1.359(7)
C(5)-N(1)	1.416(6)
C(6)-N(2)	1.384(6)
C(6)-H(6)	0.9500
C(7)-N(1)	1.349(6)
C(7)-N(2)	1.374(6)
C(7)-Re(1)	2.129(4)
C(8)-N(3)	1.344(6)
C(8)-C(9)	1.381(7)
C(8)-N(2)	1.411(6)
C(9)-C(10)	1.385(7)
C(9)-H(9)	0.9500
C(10)-C(11)	1.382(8)
C(10)-H(10)	0.9500
C(11)-C(12)	1.380(8)
C(11)-H(11)	0.9500
C(12)-N(3)	1.355(6)
C(12)-H(12)	0.9500
C(13)-O(1)	1.154(6)
C(13)-Re(1)	1.915(5)
C(14)-O(2)	1.150(6)
C(14)-Re(1)	1.951(5)
C(15)-O(3)	1.146(6)
C(15)-Re(1)	1.910(5)
N(3)-Re(1)	2.208(4)
Br(1)-Re(1)	2.6199(5)

Bond angles [°]

C(2)-C(1)-N(1)	118.6(5)
C(2)-C(1)-H(1)	120.7
N(1)-C(1)-H(1)	120.7
C(1)-C(2)-C(3)	121.2(5)
C(1)-C(2)-H(2)	119.4
C(3)-C(2)-H(2)	119.4
C(4)-C(3)-C(2)	121.0(5)

C(4)-C(3)-H(3)	119.5
C(2)-C(3)-H(3)	119.5
C(3)-C(4)-C(5)	119.3(5)
C(3)-C(4)-H(4)	120.4
C(5)-C(4)-H(4)	120.4
C(6)-C(5)-N(1)	106.2(4)
C(6)-C(5)-C(4)	135.2(5)
N(1)-C(5)-C(4)	118.6(5)
C(5)-C(6)-N(2)	106.0(4)
C(5)-C(6)-H(6)	127.0
N(2)-C(6)-H(6)	127.0
N(1)-C(7)-N(2)	103.3(4)
N(1)-C(7)-Re(1)	140.7(3)
N(2)-C(7)-Re(1)	115.8(3)
N(3)-C(8)-C(9)	124.7(4)
N(3)-C(8)-N(2)	113.2(4)
C(9)-C(8)-N(2)	122.1(4)
C(8)-C(9)-C(10)	117.5(5)
C(8)-C(9)-H(9)	121.2
C(10)-C(9)-H(9)	121.2
C(11)-C(10)-C(9)	119.4(5)
C(11)-C(10)-H(10)	120.3
C(9)-C(10)-H(10)	120.3
C(12)-C(11)-C(10)	119.1(5)
C(12)-C(11)-H(11)	120.4
C(10)-C(11)-H(11)	120.4
N(3)-C(12)-C(11)	122.8(5)
N(3)-C(12)-H(12)	118.6
C(11)-C(12)-H(12)	118.6
O(1)-C(13)-Re(1)	177.5(5)
O(2)-C(14)-Re(1)	177.8(5)
O(3)-C(15)-Re(1)	177.9(5)
C(7)-N(1)-C(1)	126.8(4)
C(7)-N(1)-C(5)	111.8(4)
C(1)-N(1)-C(5)	121.4(4)
C(7)-N(2)-C(6)	112.7(4)
C(7)-N(2)-C(8)	119.3(4)
C(6)-N(2)-C(8)	128.0(4)
C(8)-N(3)-C(12)	116.4(4)
C(8)-N(3)-Re(1)	117.5(3)
C(12)-N(3)-Re(1)	126.0(3)
C(15)-Re(1)-C(13)	87.4(2)
C(15)-Re(1)-C(14)	91.9(2)
C(13)-Re(1)-C(14)	89.8(2)
C(15)-Re(1)-C(7)	95.33(19)
C(13)-Re(1)-C(7)	100.16(19)
C(14)-Re(1)-C(7)	167.9(2)
C(15)-Re(1)-N(3)	91.48(18)
C(13)-Re(1)-N(3)	174.05(18)
C(14)-Re(1)-N(3)	96.07(19)
C(7)-Re(1)-N(3)	74.11(16)

C(15)-Re(1)-Br(1)	177.35(16)
C(13)-Re(1)-Br(1)	95.01(15)
C(14)-Re(1)-Br(1)	87.03(15)
C(7)-Re(1)-Br(1)	85.31(12)
N(3)-Re(1)-Br(1)	86.22(10)

Table S5. Properties of some of the more intense electronic transitions computed for *fac*-[Re(pyipy)$(CO)_3$Cl] (**1**). In the electronic density difference maps (EDDMs), cyan and violet indicates a decrease and increase in electron density, respectively.

S_n	*E* [eV]	λ [nm]	*f*			EDDM
1	2.982	416	0.0531	HOMO→LUMO	93%	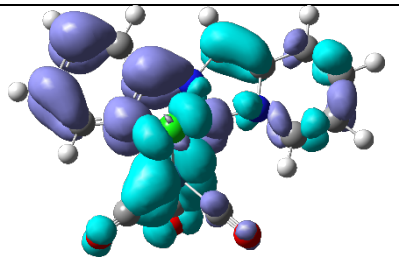 $S_0 \rightarrow S_1$
2	3.325	373	0.0641	HOMO–1→LUMO	92%	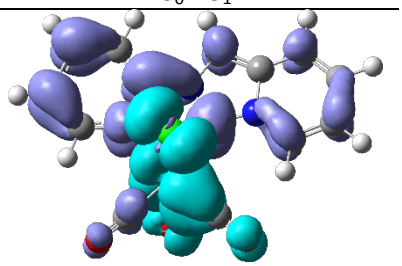 $S_0 \rightarrow S_2$
14	4.679	265	0.1285	HOMO–4→LUMO HOMO–2→LUMO+2	55% 9%	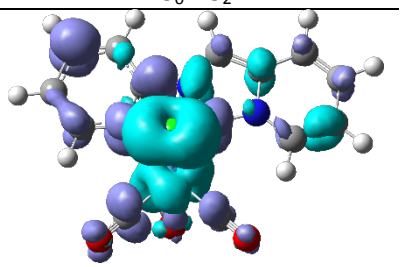 $S_0 \rightarrow S_{14}$
17	4.867	255	0.1033	HOMO–2→LUMO+2	72%	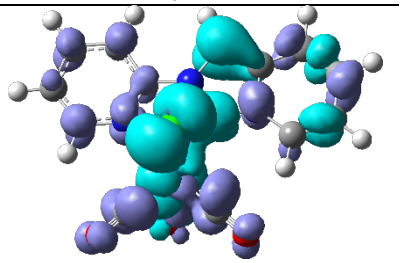 $S_0 \rightarrow S_{17}$
21	5.138	241	0.1813	HOMO–2→LUMO+3 HOMO–6→LUMO HOMO→LUMO+5	34% 13% 9%	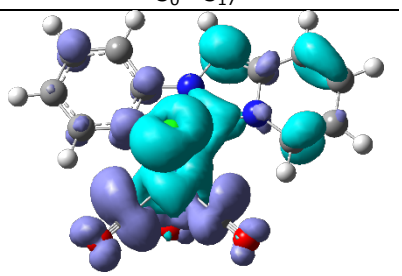 $S_0 \rightarrow S_{21}$

Table S6. Properties of some of the more intense electronic transitions computed for *fac*-[Re(pyipy)$(CO)_3$Br] (**2**). In the electronic density difference maps (EDDMs), cyan and violet indicates a decrease and increase in electron density, respectively.

S_n	*E* [eV]	λ [nm]	*f*			EDDM
1	2.975	417	0.0511	HOMO→LUMO	92%	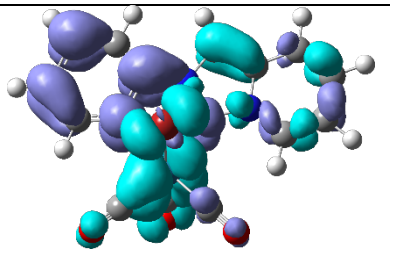 $S_0 \rightarrow S_1$
2	3.278	378	0.0524	HOMO–1→LUMO	92%	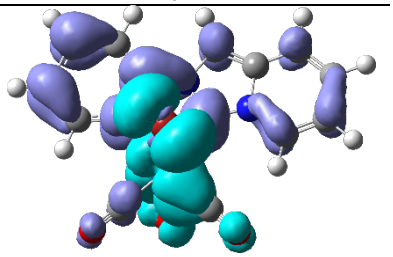 $S_0 \rightarrow S_2$
15	4.616	269	0.0916	HOMO–5→LUMO HOMO–1→LUMO+2	71% 13%	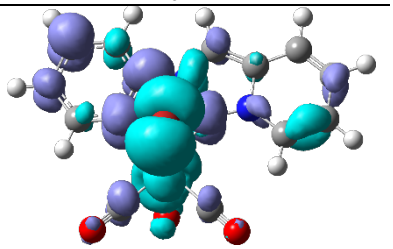 $S_0 \rightarrow S_{15}$
18	4.800	258	0.0901	HOMO–6→LUMO HOMO→LUMO+5	73% 10%	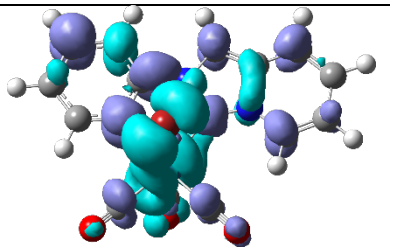 $S_0 \rightarrow S_{18}$